Linearization of an Oceanic General Circulation Model for Data Assimilation and Climate Studies

DIMITRIS MENEMENLIS AND CARL WUNSCH

Earth, Atmospheric and Planetary Sciences, Massachusetts Institute of Technology, Cambridge, Massachusetts

(Manuscript received 4 May 1995, in final form 10 January 1996)

ABSTRACT

A recipe for the linearization and state reduction of a general circulation model (GCM) is evaluated in a North Pacific test basin. The underlying assumption is that modern GCMs are, or will become, sufficiently accurate so that large-scale differences with the real ocean are small and have linear physics. Model Green's functions are used to construct a reduced-order linear model that compares favorably with the large-scale response of the GCM away from the western boundary. In a numerical example, the linear model is applied to the estimation of the large-scale internal structure of a simulated ocean using pseudotomographic and altimetric measurements. The sensitivity of the solution to a priori statistical assumptions is analyzed. Several algorithmic improvements are explored to render the estimation procedure more efficient, more accurate, and easier to implement than in previous studies.

1. Introduction

We evaluate the response of a general circulation model (GCM) to large-scale density perturbations in the North Pacific and construct a simple linear model that approximately describes the time evolution of these perturbations. This study is of interest both because it provides insight in the large-scale response of the model ocean and because of the possible use of the linear model for data assimilation leading to improved estimates of oceanic climate. The study was initiated in anticipation of long-range tomographic measurements to be made by the Acoustic Thermometry of Ocean Climate (ATOC) project in the North Pacific. An example is presented using simulated tomographic and altimetric observations.

A fundamental requirement for monitoring oceanic climate and climate shift is the separation of the large, slow scales of oceanic variability from the mesoscale and other short-term variability. This separation of scales is often performed using low-pass filters (Levitus et al. 1994; Parrilla et al. 1994; Roemmich 1992) or objective analysis procedures (Bindoff and Wunsch 1992; Fukumori and Wunsch 1991; Levitus 1990). But the expected amplitude of the climate signal is small relative to the natural variability, and the available observations are scarce and disparate. Our objective is to improve the estimates of oceanic climate by combining the available observations with a modern GCM.

The optimal combination of oceanic data and models is extensively discussed by Wunsch (1996), Bennett (1992), Ghil and Malanotte-Rizzoli (1991), and references therein. The most successful estimation methods, that is, the ones that can provide optimal state estimates and error statistics, are applicable to linear or linearized problems. However, most oceanographic and other real-world problems are intrinsically nonlinear.

Another complication is the computational burden of the estimation algorithms. The complete characterization of the error statistics requires the storage and manipulation of a covariance matrix with a dimension equaling the square of the model state. For example, one of the models used in the current study has a state size of 10^6, which is modest by modern GCM standards. This model requires 1 h of processing time per year of integration at a sustained rate of 1 Gflop s^{-1}. The error covariance matrix would have 10^{12} elements and require on the order of 100 yr of processing time per year of integration for its computation. Hence, the brute-force solution of the estimation problem is impractical for the foreseeable future, even with the anticipated availability of teraflop-per-second supercomputers.

For the above reasons, the art of data assimilation often resides in finding ways to linearize and reduce the dimensions of the problem at hand. Fukumori and Malanotte-Rizzoli (1995), and Stammer and Wunsch (1996) provide recent examples of practical estimation methods for use with large nonlinear GCMs. The former is a sequential method based on a reduced-order steady-state, linearized Kalman filter. The latter is a ''whole

Corresponding author address: Dr. Dimitris Menemenlis, Earth, Atmospheric, and Planetary Sciences, Massachusetts Institute of Technology, Building 54, Rm. 1511, Cambridge, MA 02139-4307.
E-mail: dimitri@gulf.mit.edu

© 1997 American Meteorological Society

domain'' inversion based on the computation of model Green's functions. Although the two approaches were applied to different domains and dynamical regimes, they both make use of reduced effective model dimensions and of time-invariant linearization of the dynamical model.

The current study is an extension of the work reported by Stammer and Wunsch (1996). They used a 4-level, 1° North Pacific realization of the Geophysical Fluid Dynamics Laboratory (GFDL) model and constrained it to consistency with a year of TOPEX/Poseidon altimetric data. They linearized the numerical model by computing its response to a series of isolated, geostrophically balanced vortices. The resulting Green's functions provided the kernels for a whole domain linear inverse problem. The perturbation analysis is repeated here at higher vertical resolution, 20 levels instead of 4. In addition to the GFDL model, we also make use of a new GCM developed at the Massachusetts Institute of Technology (MIT). The Green's functions computations are initialized using large-scale density perturbations instead of large-scale vortices. This approach excites a predominantly baroclinic response and is better suited to the study of the large, slow scales of oceanic variability. The baroclinic response is very sensitive to the details of the internal oceanic structure, while the depth-averaged response is sensitive to surface wind forcing and topography.

The model Green's functions can be represented efficiently by a state-transition matrix instead of the explicit storage of a set of response functions. For typical problems, the former representation reduces the computational cost and storage requirements of the Green's functions by more than an order of magnitude, and the estimation problem can be solved by a sequential filter/smoother formalism instead of a whole domain approach. The increased efficiency greatly extends the size of problems that can be tackled with currently available computational resources.

The remaining discussion is organized as follows. The climate estimation problem is formally defined in section 2. Section 3 is a brief description of the GCMs used in the current study. The response of the MIT GCM to internal density perturbations is discussed in section 4, setting the stage for the state-reduction approximation of section 5. Two methods for obtaining a linearized model are presented in section 6. In section 7 we provide a numerical example of the estimation problem using simulated altimetric and tomographic measurements, and we evaluate the sensitivity of the solution to a priori statistical assumptions.

2. Problem statement

Let $\boldsymbol{\xi}(t)$ represent the state of the ocean at some time t and $\hat{\boldsymbol{\xi}}(t)$ be an estimate of this state provided by a numerical model. For example, the state vector of the MIT GCM described in section 3a comprises temperature, salinity, and three components of velocity at each grid point. Algebraically, the GCM can be described as a rule for stepping the state vector forward,

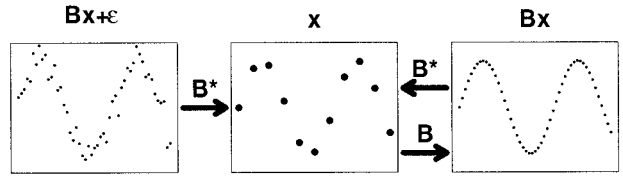

FIG. 1. Schematic representation of the interpolation and state reduction operators.

$$\hat{\boldsymbol{\xi}}(t+1) = \mathcal{F}[\hat{\boldsymbol{\xi}}(t), \mathbf{w}(t)], \tag{1}$$

where $\mathbf{w}(t)$ represents boundary conditions and model parameters at time t. We make the fundamental assumption that for large scales, the difference between the true and model states,

$$\mathbf{x}(t) \equiv \mathbf{B}^*[\boldsymbol{\xi}(t) - \hat{\boldsymbol{\xi}}(t)], \tag{2}$$

is sufficiently small so that the physics of $\mathbf{x}(t)$ are essentially linear:

$$\mathbf{x}(t + \delta t) = \mathbf{A}(t)\mathbf{x}(t) + \mathbf{q}(t), \tag{3}$$

where $\mathbf{x}(t)$ is the reduced state vector, $\mathbf{A}(t)$ is the state transition matrix, $\mathbf{q}(t)$ is the control variable that accounts for model error, and δt represents the linearized model time step that in practice can be considerably longer than the time step of the GCM. We use $\delta t = 30$ days for the linearized model and 1-h time steps to integrate the MIT and the GFDL models.

Matrix $\mathbf{B}^*$ represents the state reduction operator that projects the perturbations onto some truncated basis set (see Fukumori and Malanotte-Rizzoli 1995). Here, it may be thought of as a filter that attenuates mesoscale noise to capture the ocean-climate signal. A pseudo-inverse operator $\mathbf{B}$ is also defined such that

$$\mathbf{B}^*\mathbf{B} = \mathbf{I}, \qquad \mathbf{B}\mathbf{B}^* \neq \mathbf{I}, \tag{4}$$

so that it is possible to write

$$\boldsymbol{\xi}(t) - \hat{\boldsymbol{\xi}}(t) = \mathbf{B}\mathbf{x}(t) + \boldsymbol{\epsilon}(t). \tag{5}$$

Here, $\mathbf{B}$ is an interpolation operator that maps the reduced state vector back onto the original grid, $\mathbf{I}$ is the identity matrix, and $\boldsymbol{\epsilon}(t)$ represents the high-frequency/wavenumber components that lie in the null space of the transformation

$$\mathbf{B}^*\boldsymbol{\epsilon}(t) = \mathbf{O}, \tag{6}$$

with $\mathbf{O}$ being the zero matrix (see Fig. 1). A specific example and more complete discussion of the state reduction approximation follow in section 5.

The linearized model in (3) implies that large-scale perturbations described by the reduced state vector $\mathbf{x}(t)$ are approximately dynamically decoupled from the unresolved scales $\boldsymbol{\epsilon}(t)$; that is,

$$\mathbf{B}^*\mathcal{F}[\hat{\boldsymbol{\xi}}(t) + \boldsymbol{\epsilon}(t), \mathbf{w}(t)] \sim \mathbf{B}^*\mathcal{F}[\hat{\boldsymbol{\xi}}(t), \mathbf{w}(t)]. \tag{7}$$

TABLE 1. Description and definition of estimation matrices.

Name	Description	Definition
$\mathbf{A}$	Linear model	$\mathbf{x}(t + \delta t) = \mathbf{A}\mathbf{x}(t) + \mathbf{q}(t)$
$\mathbf{B}^*$	State reduction	$\mathbf{x}(t) = \mathbf{B}^*[\boldsymbol{\xi}(t) - \hat{\boldsymbol{\xi}}(t)]$
$\mathbf{B}$	Interpolation	$\mathbf{B}^*\mathbf{B} = \mathbf{I}$, $\mathbf{B}\mathbf{B}^* \neq \mathrm{I}$
$\mathbf{E}$	Measurement model	$\mathbf{y}(t) = \mathbf{E}\mathbf{B}\mathbf{x}(t) + \mathbf{n}(t)$
$\mathbf{P}$	Uncertainty matrix	$\mathbf{P} = \langle(\hat{\mathbf{x}} - \mathbf{x})(\hat{\mathbf{x}} - \mathbf{x})^{\mathrm{T}}\rangle$
$\mathbf{Q}$	System error	$\mathbf{Q} = \langle\mathbf{q}\mathbf{q}^{\mathrm{T}}\rangle$
$\mathbf{R}$	Measurement error	$\mathbf{R} = \langle\mathbf{n}\mathbf{n}^{\mathrm{T}}\rangle$
$\mathbf{S}$	State covariance	$\mathbf{S} = \langle\mathbf{x}\mathbf{x}^{\mathrm{T}}\rangle$

The validity of this assumption for the North Pacific is tested in sections 4 and 6 using the MIT and the GFDL models.

Most measurements can be represented as some linear combination of the state vector $\boldsymbol{\xi}(t)$ plus noise $\boldsymbol{\nu}(t)$;

$$\boldsymbol{\eta}(t) = \mathbf{E}(t)\boldsymbol{\xi}(t) + \boldsymbol{\nu}(t). \tag{8}$$

Typically, matrix $\mathbf{E}$ is sparse with only a few nonzero elements corresponding to the measurement locations. As discussed in section 7, ocean acoustic tomography and satellite altimetry provide path and depth-integrated information, respectively. In the current discussion, it is convenient to define the observed difference between the measurements and the GCM prediction:

$$\mathbf{y}(t) = \boldsymbol{\eta}(t) - \mathbf{E}(t)\hat{\boldsymbol{\xi}}(t) \tag{9}$$

$$= \mathbf{E}(t)\mathbf{B}\mathbf{x}(t) + \mathbf{n}(t). \tag{10}$$

In (10), the observed difference $\mathbf{y}(t)$ is expressed in terms of the reduced state $\mathbf{x}(t)$. The noise term $\mathbf{n}(t)$ now includes a term due to small-scale, high-frequency variability $\boldsymbol{\epsilon}(t)$ in the null space of $\mathbf{B}$, as well as measurement error $\boldsymbol{\nu}(t)$ from (8);

$$\mathbf{n}(t) = \mathbf{E}(t)\boldsymbol{\epsilon}(t) + \boldsymbol{\nu}(t). \tag{11}$$

In practice, $\boldsymbol{\nu}(t)$ is often negligible relative to the sampling error $\mathbf{E}(t)\boldsymbol{\epsilon}(t)$ in (11). It should be pointed out that in an analogous manner, $\boldsymbol{\nu}(t)$ contains a contribution due to the unresolved scales and missing physics of the GCM.

The problem consists in solving for $\hat{\mathbf{x}}(t)$, the reduced state estimate, and its uncertainty, $\mathbf{P} = \langle(\hat{\mathbf{x}} - \mathbf{x})(\hat{\mathbf{x}} - \mathbf{x})^{\mathrm{T}}\rangle$, given measurements $\mathbf{y}(t)$ and a priori covariance matrices $\mathbf{Q} = \langle\mathbf{q}\mathbf{q}^{\mathrm{T}}\rangle$, $\mathbf{R} = \langle\mathbf{n}\mathbf{n}^{\mathrm{T}}\rangle$, and $\mathbf{S} = \langle\mathbf{x}\mathbf{x}^{\mathrm{T}}\rangle$. The caret indicates an estimate, the angle brackets represent an ensemble average, and superscript T is the transpose operator. Solutions for the above problem are readily available in the literature. The real challenge lies in defining matrices $\mathbf{A}$, $\mathbf{B}^*$, $\mathbf{E}$, $\mathbf{Q}$, $\mathbf{R}$, and $\mathbf{S}$ (see Table 1). This study pertains to the definition of $\mathbf{A}$ and $\mathbf{B}^*$, the linear model, and the state reduction operator, respectively. The consequences of using wrong a priori $\mathbf{Q}$, $\mathbf{R}$, and $\mathbf{S}$ are explored in section 7.

3. Model description

The current study was initiated using the GFDL numerical code and model output from a global eddy-resolving integration by Semtner and Chervin (1992). These results are reported in sections 6 and 7. We have now switched over to the newly developed MIT GCM. This model is used to carry out the perturbation analysis reported in section 4 and will be the focus of our future assimilation efforts. The above models and their configurations are briefly described below.

a. MIT model

In its current configuration, the MIT GCM (Marshall et al. 1997a,b) solves the incompressible Navier–Stokes equations in spherical geometry, has a rigid lid, and employs an equation of state appropriate to sea water. Height is used as a vertical coordinate, and the model can handle arbitrarily complex coastlines, islands, and bathymetry. The model relaxes the hydrostatic approximation but retains a ''hydrostatic switch'' that, if desired, turns off nonhydrostatic terms for use in large-scale modeling. It is prognostic in three components of velocity, temperature, and salinity and diagnostic in pressure. A finite volume, predictor–corrector numerical procedure is used on a staggered (Arakawa ''C'') grid. The model is implemented on parallel machines.

For this study, the MIT GCM is integrated in hydrostatic mode for the Pacific Ocean. It has realistic coastlines and bottom topography (Fig. 2). Bottom and side walls are insulating. A no-slip side wall condition is imposed and the bottom is free slip. The model domain extends from 30°S to 61°N, meridionally, and from 123° to 292°E, zonally, with horizontal grid spacing of 1°. There are 20 vertical levels (see Table 2), to a maximum depth of 5302 m. At the surface, the model is relaxed to climatological values of temperature and salinity with a relaxation timescale of 25 days. At the southern boundary, the relaxation occurs over a 500-km zone with a timescale of 5 days at the boundary decreasing linearly to 100 days at 500 km.

The model was initialized from climatological annual mean temperature and salinity distributions (Levitus 1982), and a resting flow field. It was integrated for 17 years with annual mean temperature, salinity, and surface wind forcing. From year 18 onward, monthly temperatures and seasonal salinities were used, and the surface was forced with the monthly winds provided by Trenberth et al. (1989). The forcing fields were updated every 24 h using linear interpolation from the monthly or seasonal values. Surface heat and freshwater fluxes from Oberhuber (1988) were introduced in the surface layer starting on year 29, while continuing to relax to climatological temperature and salinity. The model time step is 1 h. Table 3 lists the mixing and diffusion coefficients.

Figure 3 displays the pressure and velocity fields at the 38-m depth, after 43 years of integration. The major climatological circulation components of the North Pacific can be recognized (compare to Pickard and Emery 1990, Fig. 7.31). They include the Kuroshio and the

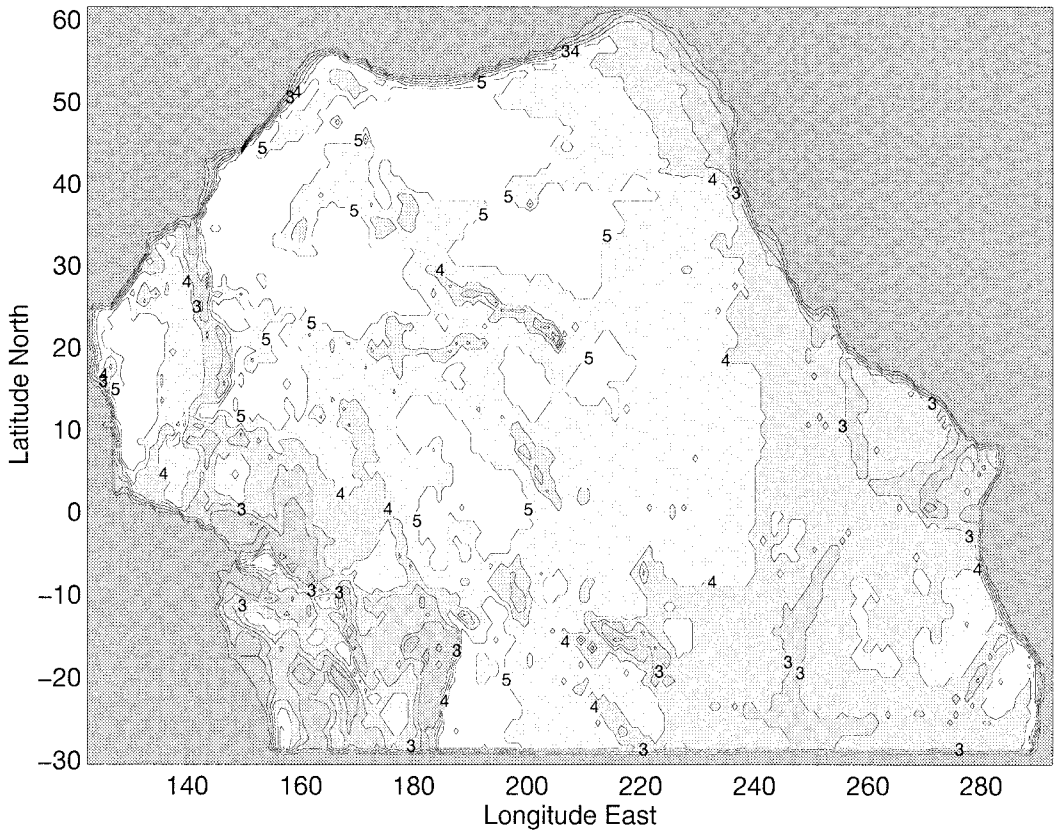

FIG. 2. Coastlines and bottom topography used to integrate the MIT GCM. Contour interval is 1 km.

Oyashio Currents, which join to give rise to the North Pacific Current, the California Current, and the North Equatorial Current. These current systems are part of the North Pacific Gyre, and to the north, the Alaskan Gyre. The model also reproduces the South Equatorial Current, which straddles the equator, the Equatorial Countercurrent centered at 7°N, and just below the surface the Equatorial Undercurrent (see Fig. 4). Figure 5 displays temperature, salinity, and density profiles averaged over the model domain. There is a net influx of heat at the boundaries and the model gets progressively warmer, with a maximum warming of 2°C at 300 m after 43 years of integration: tracer profile gradients are severely eroded. The conclusion is that the model adequately reproduces the large-scale wind-driven circulation but fails to properly represent the small-scale processes responsible for interior property distributions. Work is under way to address these gross model errors by improving the parameterization of mixed layer dynamics and mixing processes in the interior. Nevertheless, the model as it stands suffices for the current numerical study.

TABLE 2. MIT GCM vertical levels definition for the 20-layer North Pacific integration.

Depth (dbar)	Depth (m)	Spacing (dbar)	Depth (dbar)	Depth (m)	Spacing (dbar)
12.5	12.7	25	847.5	864.1	275
37.5	38.2	25	1160	1183	350
62.5	63.7	25	1542	1573	415
87.5	89.2	25	1975	2014	450
117.5	119.8	35	2450	2498	500
160	163.1	50	2950	3008	500
222.5	226.9	75	3450	3518	500
310	316.1	100	3950	4027	500
435	443.5	150	4450	4537	500
610	621.9	200	4950	5047	500

b. *Bryan–Cox model*

The linear model discussed in section 6 was obtained using the GFDL GCM (Bryan 1969; Cox 1984) in the configuration described by Stammer and Wunsch (1996). The model has 1° horizontal grid spacing and

TABLE 3. MIT GCM mixing and diffusion coefficients for the North Pacific integration.

Parameter	Years 1–33 ($m^2\ s^{-1}$)	Years 34–43 ($m^2\ s^{-1}$)
Horizontal mixing	10^4	5×10^3
Horizontal diffusion	10^3	10^3
Vertical mixing	10^{-2}	10^{-3}
Vertical diffusion	5×10^{-5}	3×10^{-5}

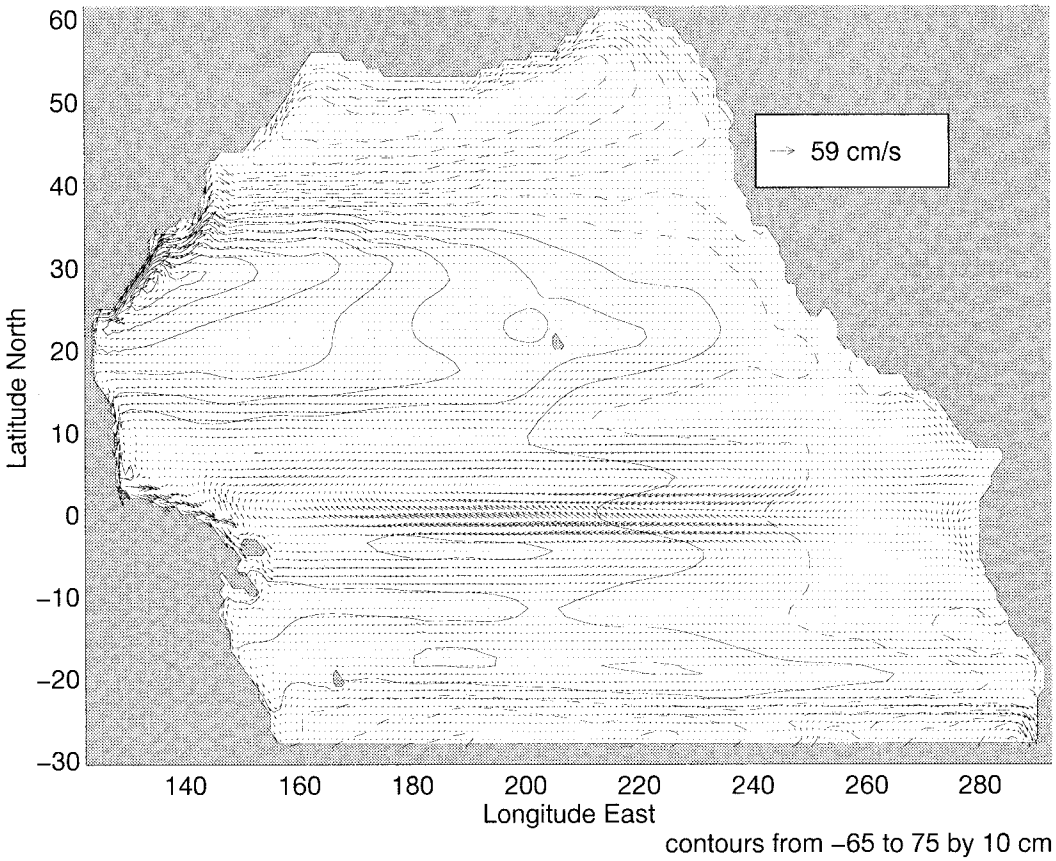

FIG. 3. Pressure and horizontal velocity at the 38-m depth for the MIT GCM following the 42-yr spinup period. As discussed in the text, the model reproduces the major North Pacific circulation patterns.

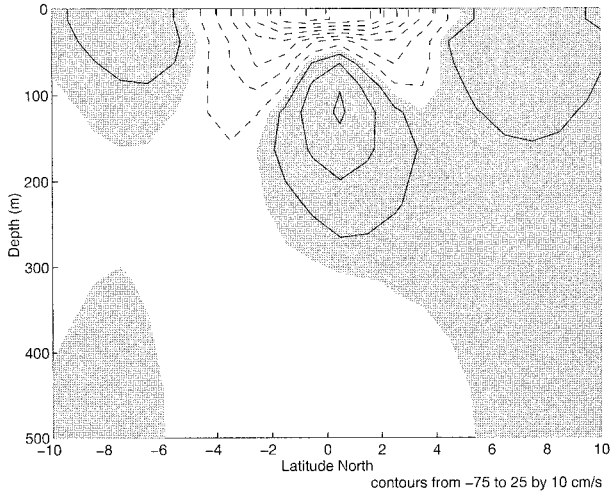

FIG. 4. Meridional section of zonal velocity near the equator at 222°E. Shaded areas and solid contour lines indicate eastward flow. The model resolves the South Equatorial Current, the Equatorial Countercurrent, and the Equatorial Undercurrent.

four vertical levels of thickness 100, 500, 1000, and 2400 m, respectively, to a maximum depth of 4000 m. It was spun up for 23 years in the Pacific Ocean north of 30°S. As discussed by Stammer and Wunsch (1996) this model simulated the major components of the North Pacific circulation described earlier. However, the model does not resemble observations in the Tropics due to the low vertical resolution.

The state estimation example discussed in section 7 was carried out using output from a global implementation of the Bryan–Cox primitive equation model with nominal grid spacing of ¼° in the horizontal and 20 levels in the vertical (Semtner and Chervin 1992).

4. Perturbation analysis

The response of the MIT model to internal midlatitude temperature perturbations is evaluated. This problem is related to that of forced oceanic waves and geostrophic adjustment, which is extensively discussed in the lit-

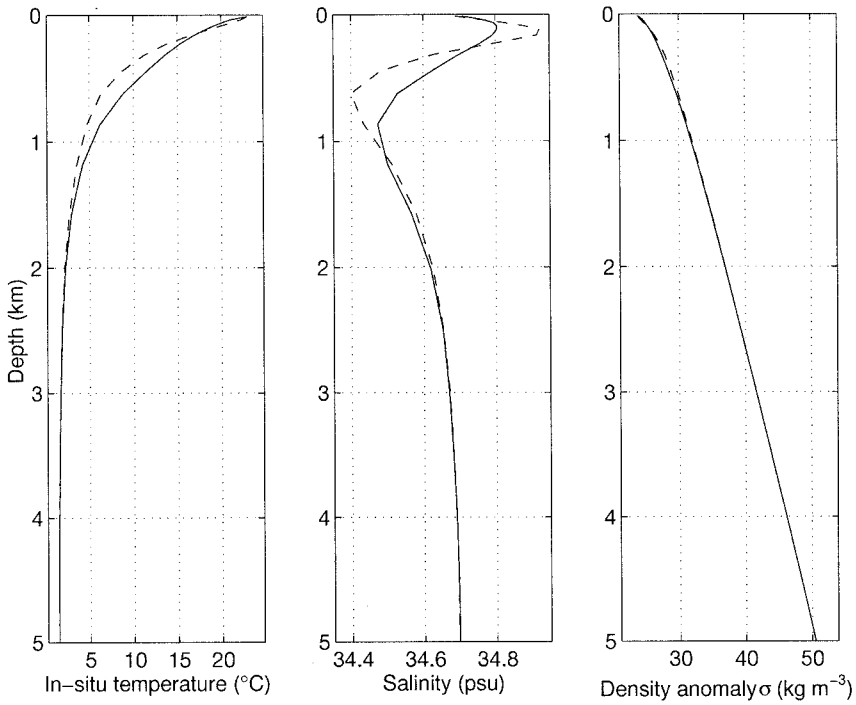

FIG. 5. Model temperature, salinity, and density profiles. The dashed lines are the initial basin-averaged profiles taken from Levitus (1982). The solid lines represent annual mean values during year 43.

erature (see Gill 1982; Philander 1978; Blumen 1972; and references therein). The difference is that the GCM provides solutions that include the effect of realistic topography, stratification, horizontal gradients, and mean circulation. The objective is to obtain guidelines for the state reduction approximation and model linearization to be discussed in subsequent sections. In particular, the extent to which the large, slow scales of the model response are dynamically coupled to the smaller or faster features resolved by the model needs to be determined.

Following the 43-yr spinup described in section 3, the MIT GCM was integrated for an additional 2 yr with monthly forcing. This 2-yr integration provides the reference state for the perturbation analysis. Starting at the beginning of this period, temperature anomalies are introduced in the model. The model is then integrated with the same boundary conditions and model parameters as before and the time evolution of the perturbations relative to the reference state is recorded.

The first experiment studies the model response to the warming of a lens of water centered at 34.5°N, 209.5°E at a depth of 350 m. The perturbation has horizontal extent of 16° (~1600 km), both zonally and meridionally, and a vertical extent of 500 m. It is tapered by a Hanning (cosine) window in all three directions with a maximum perturbation of 0.1°C at the center. No attempt was made to introduce the corresponding geostrophic velocity perturbation because, as is shown below, the geostrophic adjustment transients can be neglected.

Figure 6 shows surface pressure and horizontal velocity during the geostrophic adjustment period. The flow is initially downgradient but, as expected, it comes to complete geostrophic equilibrium within 20 to 25 inertial periods (~21 h at that latitude) (see Gill 1982, section 7.3). Inertial oscillations associated with the radiation of inertia–gravity waves from the region are clearly seen in Fig. 6. The geostrophically adjusted state is that of a warm core anticyclonic eddy, overlying cyclonic circulation caused by vortex stretching as the lighter water rises to its new equilibrium position. From geostrophic considerations, the strength of the surface velocity perturbation is

$$\delta v_s \sim \frac{g\delta z\delta\rho}{f\rho\delta x} = 0.07 \text{ cm s}^{-1}, \tag{12}$$

where $g = 9.8$ m s^{-2} is the acceleration due to gravity; $\delta z = 500$ m and $\delta x = 1600$ km are the vertical and horizontal length scales of the disturbance, respectively; $f = 8 \times 10^{-5}$ s^{-1} is the Coriolis parameter; and $\delta\rho/\rho = 1.7 \times 10^{-5}$ is the fractional density change corresponding to a 0.1°C warming at that depth. The underlying cyclonic perturbation is such that the depth-integrated velocity is approximately zero so that the velocity perturbation below the temperature anomaly is

$$\delta v_b \sim h_1\delta v_s/h_2 = 0.005 \text{ cm s}^{-1}, \tag{13}$$

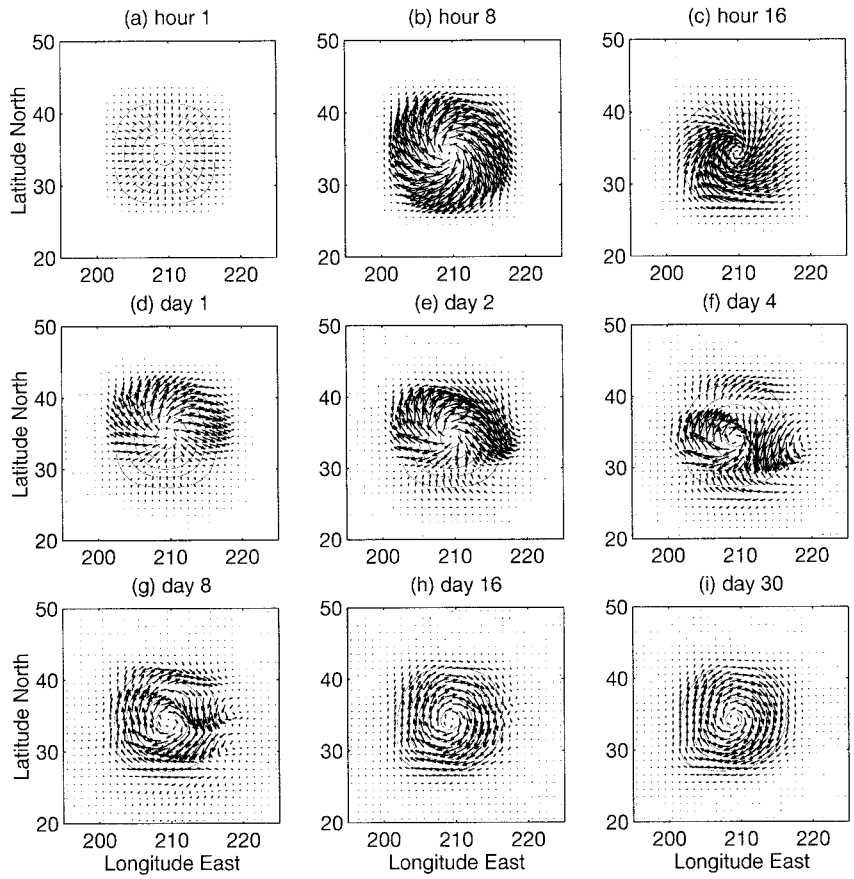

FIG. 6. Surface pressure and horizontal velocity during the geostrophic adjustment period following the introduction of a warm lens centered at 34.5°N, 209.5°E, and 350-m depth. Contours are from 0.05 to 0.45 by 0.1 cm. A maximum speed of 0.21 cm s^{-1} is observed at hour 8, and subsequently decays to 0.11 cm s^{-1} on day 30.

where $h_1 = 350$ m and $h_2 = 4650$ m represent the height of the water column above and below the disturbance, respectively. In the model, the depth-integrated perturbation velocity is nonzero because of residual terms from the geostrophic adjustment process ($\sim 10^{-6}$ cm s^{-1}) and because of nonlinear flow interaction with bottom topography, horizontal density gradients, and the mean circulation ($\sim$0.01 cm s^{-1}). The contribution from the geostrophic adjustment process is negligible. However, the topographic and other nonlinear effects are of the same order of magnitude as the cyclonic flow below the perturbation and they cannot be neglected. Its spatial structure would be difficult to predict from theoretical considerations alone, but it is readily provided by the numerical model.

In an analogous manner to geostrophic adjustment, but on much longer timescales, the model ocean returns to local Sverdrup balance by radiating Rossby waves away from the perturbed region (e.g., Gill 1982, section 12.4). Figures 7a and 8a show the model response at the end of month 16. The pattern is characteristic of long westward propagating baroclinic Rossby waves (see Gill 1982, section 12.3). The waves exhibit the expected decrease in phase speed with increasing latitude (the southwest-northeast slope of the patterns), but are modified by complex interactions with topography, horizontal density gradients, and the mean flow field (note the southeast drift of the pattern relative to the initial location of the disturbance). The observed phase speed of the first baroclinic mode is $c \sim 3$ cm s^{-1} at 34.5°N, which suggests an internal radius of deformation $L_D \sim (c/\beta)^{1/2} \sim 40$ km, where $\beta = 1.9 \times 10^{-11}$ m^{-1} s^{-1} is the variation of the Coriolis parameter with latitude. Higher baroclinic modes have progressively slower phase speeds, causing the separation of the disturbance into several baroclinic modes. Finally, we note that the contribution of salinity to the density perturbation is not insignificant. For example, a salinity change of order 0.005 psu is observed near the surface at the end of month 16, compared to a temperature perturbation of order 0.05°C. These correspond to density perturbations of order 0.0035 and 0.01 kg m^{-3}, respectively. On average, the net effect of changes in model salinity is to decrease the total density perturbation due to the temperature anomaly.

To verify that the geostrophic adjustment transients do

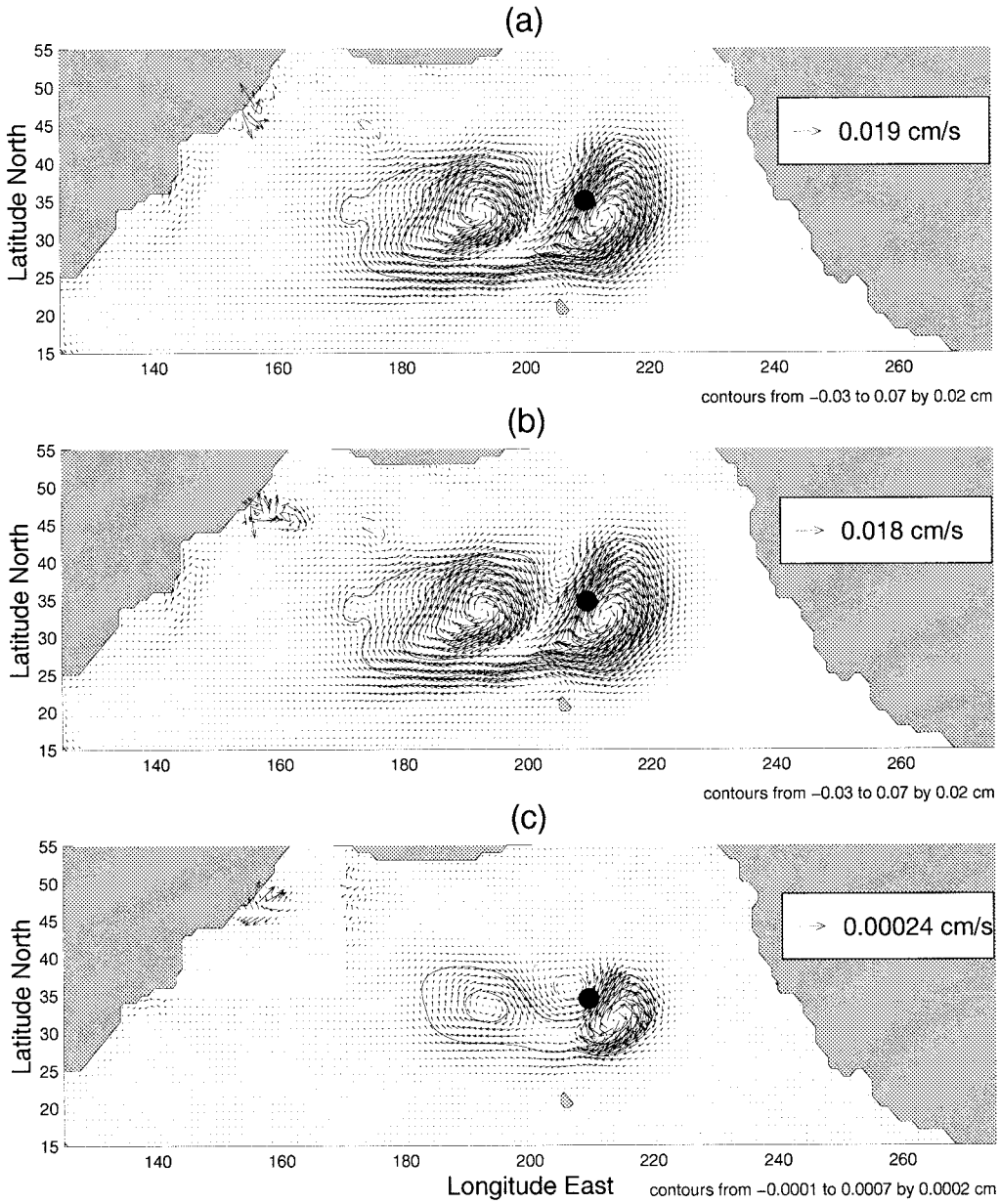

FIG. 7. Model pressure and horizontal velocity at the 316-m depth: (a) 16-month response to a large-scale temperature perturbation at 34.5°N, 209.5°E, and 350-m depth; (b) same as in (a), but the velocity and salinity fields were returned to the reference level at the end of the first month; (c) 16-month response to a localized temperature perturbation (the upper left-hand corner of the domain, north of 35°N and west of 170°E, has been scaled down by a factor of 20). The heavy dots indicate the initial location of the disturbances. As discussed in the text, the agreement between the three cases away from the western boundary suggests that the geostrophic adjustment transients have little effect on the evolution of the perturbations, and that the large, slow scales of the model response are effectively decoupled from the smaller scales.

not influence the large-scale model response, the model was perturbed with the same temperature anomaly as before, but the velocity and salinity fields were returned to the reference state at the end of the first month. This initiates a second adjustment period. The resulting model response at the end of month 16 is shown in Fig. 7b. Except near the western boundary, the pattern is almost indistinguishable from that of the previous experiment. In the Kuroshio region, the model response is very sensitive to small perturbations because of the strong currents and density gradients. The similarity of Figs. 7a and 7b is not surprising because a large fraction of the energy of long planetary waves is in potential form. For Rossby waves with wavelength $\lambda > 1000$ km [Gill 1982, Eq. (12.3.9)]

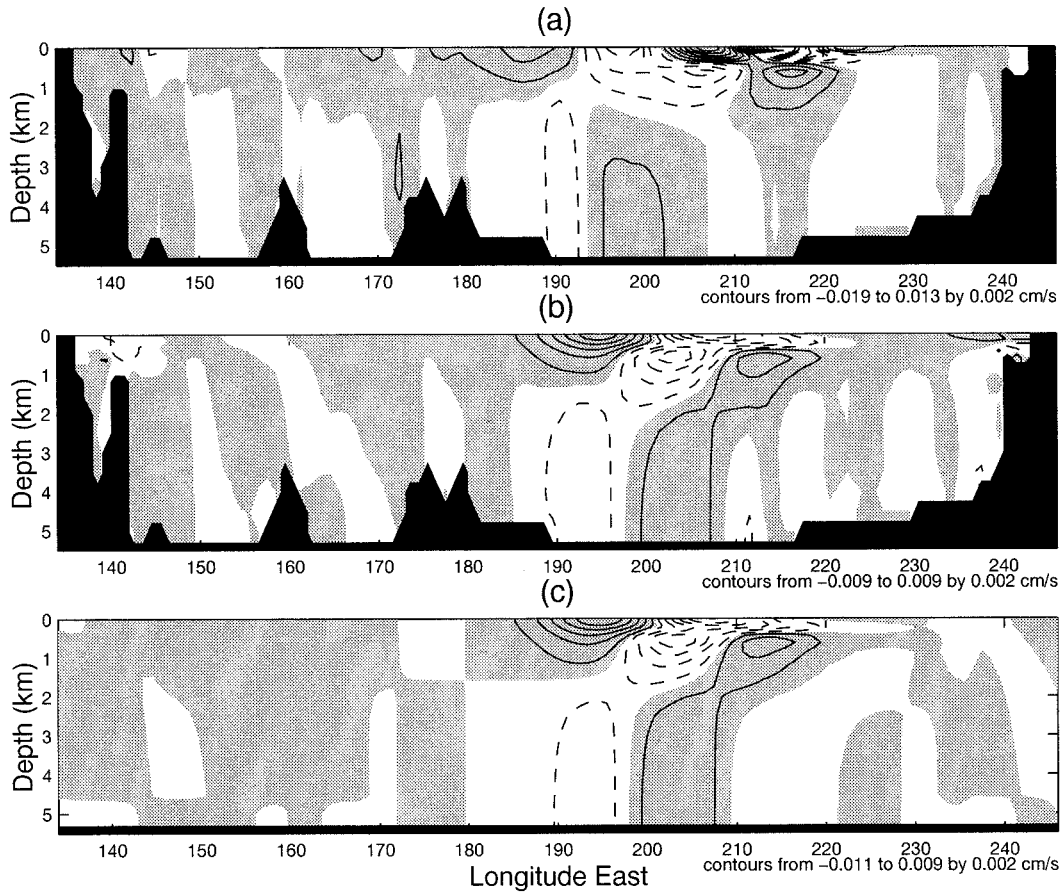

FIG. 8. Zonal section of meridional velocity at 34.5°N. Shaded areas and solid contour lines indicate northward flow. (a) Zonal section through the same field as in Fig. 7a. (b) Model response to the same perturbation as above, but for an unforced ocean that is initially at rest and has no horizontal temperature or salinity gradients. The initial temperature and salinity profiles for (b) were set by averaging the profiles of the realistic run in an area extending from 20° to 45°N meridionally and 170° to 230°E zonally. The important differences between (a) and (b) indicate that the model response is a sensitive function of the internal oceanic structure. (c) Same as in (b) but for a flat-bottom ocean. The resemblance of (b) and (c) means that topography plays a relatively minor role in the baroclinic response of the model ocean to near-surface density perturbations.

$$\frac{\text{kinetic energy density}}{\text{potential energy density}} = (k_h L_D)^2 < 2\%, \quad (14)$$

where $k_h = 2\pi/\lambda$ is the horizontal wavenumber.

In a third numerical experiment, the model was perturbed with a 0.1°C temperature anomaly in a single grid box at 34.5°N, 209.5°E and 350-m depth. This impulse function excites all spatial and temporal scales that can be resolved by the GCM. The response at the end of month 16 is shown in Fig. 7c. Although there are differences in the details, the large-scale response away from the Kuroshio region is clearly similar to that of previous experiments. This suggests that away from the western boundary, and for the current model configuration, the large-scale low-frequency response is effectively decoupled from smaller and faster processes. In the context of the current study, the complicated response near the western boundary can be accounted for by increasing the a priori error variance of the linear model in that region.

The particular response of the model ocean to perturbations is a sensitive function of the internal structure. For illustration, Figs. 8b,c display the response of an unforced ocean to the same perturbation as in Fig. 8a. The large differences between the realistic (Fig. 8a) and the idealized (Figs. 8b,c) cases indicate the rich information content of the response, as captured by a modern GCM. The estimation recipe to be discussed later seeks to use this information to better resolve the internal oceanic structure from a necessarily incomplete set of measurements.

5. State reduction

The total state dimension of the MIT GCM in the aforementioned configuration is 1 335 852. As discussed

earlier, the complete solution of the estimation problem would overwhelm the most powerful computers because of the need to store and manipulate the error covariance matrix. To proceed, one can have recourse to methods where the error covariance matrix is either ignored (e.g., nudging, Malanotte-Rizzoli and Young 1992) or not absolutely necessary (e.g., the adjoint method, Marotzke and Wunsch 1993). The alternative, which is discussed here, is to use optimal estimation methods on a reduced problem.

The motivation for the current work is the estimation of oceanic climate, that is, the large or slow scales of the variability, augmented where possible by a statistical description of the smaller scales. The exact location and time history of each geostrophic eddy is not required or obtainable from existing global datasets. However, it is assumed that a GCM driven by observed meteorological fields and constrained to consistency with the available data can accurately simulate the large or slow scales without having to exactly reproduce the small-scale behavior of the ocean.

The primary purpose of the state reduction operator, $\mathbf{B}^*$ in (2), is to reduce the problem size to one that is readily handled by available computing resources while preserving sufficient resolution to characterize the processes under study. A secondary requirement is that the null space of the transformation be approximately dynamically decoupled from the range space as in (7). Finally, the choice of $\mathbf{B}^*$ must be guided by sampling requirements; that is, the model state must be adequately filtered before subsampling to avoid aliasing. The pseudoinverse operator satisfying (4) is then obtained using

$$\mathbf{B} = \mathbf{B}^{*\mathrm{T}}(\mathbf{B}^*\mathbf{B}^{*\mathrm{T}})^{-1}. \tag{15}$$

Here, $\mathbf{B}^*\mathbf{B}^{*\mathrm{T}}$ will be invertible for any but the most unfortunate choice of $\mathbf{B}^*$ since the number of columns of $\mathbf{B}^*$ is much larger than the number of rows. Alternatively, the interpolation operator $\mathbf{B}$ can be defined first, and $\mathbf{B}^*$ is obtained using

$$\mathbf{B}^* = (\mathbf{B}^{\mathrm{T}}\mathbf{B})^{-1}\mathbf{B}^{\mathrm{T}}. \tag{16}$$

Again, the requirement that $\mathbf{B}^{\mathrm{T}}\mathbf{B}$ be invertible is easily satisfied. In practice, it is more convenient to apply a series of transformations to the model output rather than perform the state reduction operation in one pass. For example, one may wish to define $\mathbf{B}^*$ as

$$\mathbf{B}^* = \mathbf{B}_h^*\mathbf{B}_v^*\mathbf{B}_t^*, \tag{17}$$

where $\mathbf{B}_t^*$, $\mathbf{B}_v^*$, and $\mathbf{B}_h^*$ are time, vertical, and horizontal operators, respectively. Pseudoinverse operators $\mathbf{B}_t$, $\mathbf{B}_v$, and $\mathbf{B}_h$ can be defined as in (15), and it follows that

$$\mathbf{B} = \mathbf{B}_t\mathbf{B}_v\mathbf{B}_h. \tag{18}$$

An alternative framework is provided by digital filtering theory; $\mathbf{B}^*$ represents a filter that removes sub-Nyquist scales, and a sampler operating at twice the Nyquist rate. The interpolation operator $\mathbf{B}$ oversamples the signal back to the original rate and applies the same low-pass filter to remove unwanted harmonics (see Fig. 1).

In this study, the vertical state reduction operator $\mathbf{B}_v^*$ maps perturbations to the same four vertical levels as in Stammer and Wunsch (1996). Horizontal filtering is done using a two-dimensional fast Fourier transform (FFT) algorithm and setting to zero coefficients corresponding to wavelengths shorter than 16°. The resulting fields are then subsampled at 8° intervals, both zonally and meridionally, thus satisfying the Nyquist sampling criterion. Temporal sampling is done at 30-day intervals. This particular choice of $\mathbf{B}_v^*$, $\mathbf{B}_h^*$, and $\mathbf{B}_t^*$ is one of convenience and suffices for the current numerical study. The four vertical levels are those used in section 6 to integrate the GFDL model. The horizontal operator $\mathbf{B}_h^*$ and its pseudoinverse $\mathbf{B}_h$ can be efficiently implemented using FFTs without explicit evaluation or storage of either matrix. No time filtering is required because the fields used in the numerical examples have sufficiently red frequency spectra.

Alternative representations of the perturbation field are available. Empirical orthogonal functions (EOFs) from hydrographic casts are the preferred description for vertical structure in ocean acoustic tomography. Wavelets or climate model EOFs can be used horizontally. Temporal filtering may be required if the processes under study have frequency spectra that are not sufficiently red to avoid aliasing. A different approach consists in first defining the interpolation operator $\mathbf{B}$ rather than $\mathbf{B}^*$ (Fukumori and Malanotte-Rizzoli 1995).

In their analysis of the large-scale North Pacific circulation using satellite altimetry, Stammer and Wunsch (1996) form averages in 10° × 10° areas during 10-day periods. The 10-day interval coincides with the repeat cycle of the TOPEX/Poseidon altimeter. The vertical sampling scheme consists of depth averages at the four levels of their particular implementation of the GFDL model: 0–100, 100–600, 600–1600, and 1600–4000 m. This sampling scheme resolves variability due to the propagation of large-scale baroclinic Rossby waves, but it is unsuitable to the observation of barotropic Rossby waves at midlatitudes. Long barotropic Rossby waves have short periods. For example, at wavelengths greater than 1000 km, the midlatitude period is typically less than 23 days (Pond and Pickard 1983, section 12.10.4).

The current state reduction scheme restricts the analysis to scales larger than 16° in the horizontal and periods longer than 60 days, which is sufficient to resolve the large-scale baroclinic response of the ocean discussed in section 4. However, the fast or short variability caused by the propagation of barotropic Rossby waves is eliminated. It is appropriate, therefore, to restrict the reduced state vector to the description of density perturbations. Here, temperature is used as a proxy for density, but the salt contribution can be recovered from representative *T–S* diagrams or directly from the model Green's functions.

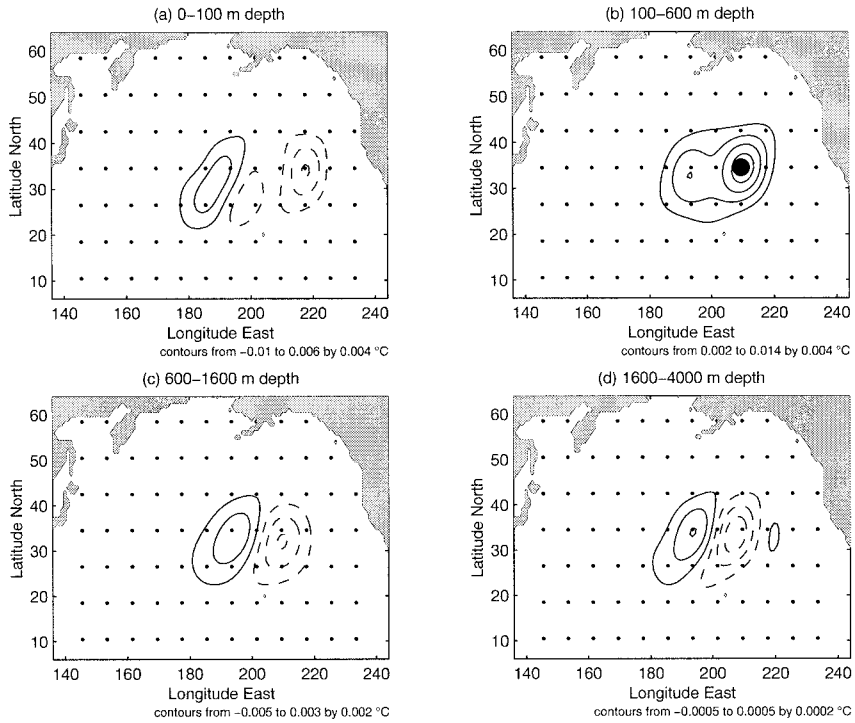

FIG. 9. Response of the four-level GFDL model to a 0.05°C perturbation, between 100- and 600-m depth, at the end of month 16. A two-dimensional low-pass spatial filter with cutoff wavelength of 16° has been applied to smooth scales not resolved by the reduced-order linear model. The heavy dot indicates the initial location of the disturbance.

6. Linearization

Two methods for deriving the state transition matrix, $\mathbf{A}$ in (3), are discussed below. The first method is based on the computation of model Green's functions and it is related to the method used by Fukumori and Malanotte-Rizzoli (1995). Model Green's functions are defined here as the GCM response to unit temperature perturbations of the reduced state vector $\mathbf{x}(t)$. These perturbations are introduced in the numerical model as $\mathbf{B}_v\mathbf{B}_h\mathbf{x}(t)$. The response of the GCM is computed as in section 4 for a single time step, δt equals 1 month, of the linear model. The GCM response is then projected back onto the reduced state vector using $\mathbf{B}^*$ and the resulting vector gives the column of the state transition matrix corresponding to the perturbed element of $\mathbf{x}(t)$. This computation, repeated for each element of $\mathbf{x}(t)$, provides the complete state transition matrix.

For illustration, the above method is used to obtain a state transition matrix for the North Pacific GFDL integration of Stammer and Wunsch (1996) (see section 3b for a brief description of model configuration). Three hundred thirty-six 30-day Green's functions are computed at the locations marked by the dots in Fig. 9 and used to define the state-transition matrix $\mathbf{A}$. Figure 9 also displays the response of the GFDL model to a 0.05°C perturbation in the second model layer at the end of month 16. The large-scale response of the GFDL model can be compared to that of the linear model in Fig. 10. The excellent correspondence between Figs. 9 and 10 indicates that the linear model $\mathbf{A}$ is able to satisfactorily reproduce the large-scale response of the fully nonlinear GCM. This result needs to be tested in eddy-resolving model configurations, but for sufficiently small perturbations, we expect this result to carry over to higher model resolutions.

A second method for obtaining $\mathbf{A}$ is related to the computation of principal oscillation patterns (e.g., von Storch 1993). Consider the response of a numerical model to some random initial perturbation field. This response, filtered by $\mathbf{B}^*$, provides a time series of the reduced state vector $\mathbf{x}(t)$, which is consistent with GCM perturbation dynamics. Right multiplication of (3) by $\mathbf{x}^{\mathrm{T}}(t)$ and taking expectations yields the state transition matrix

$$\mathbf{A} = \langle \mathbf{x}(t + \delta t)\mathbf{x}^{\mathrm{T}}(t)\rangle\langle \mathbf{x}(t)\mathbf{x}^{\mathrm{T}}(t)\rangle^{-1}, \qquad (19)$$

where it is assumed that $\mathbf{x}(t)$ and $\mathbf{q}(t)$ are uncorrelated. This method has the advantage of being able to provide an average linear model for the entire period under study rather than an exact model for a particular month.

When the covariance matrix $\langle \mathbf{x}(t)\mathbf{x}^{\mathrm{T}}(t)\rangle$ is not invertible—for example, when the number of time steps available for extracting the linear model is smaller than the dimension of $\mathbf{x}(t)$—the following inverse problem,

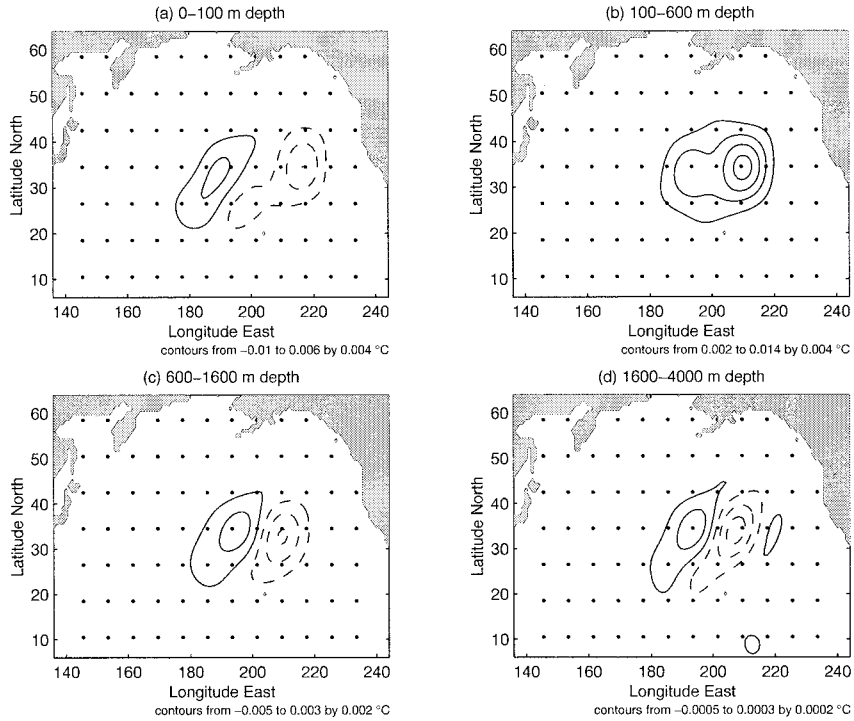

FIG. 10. Response of the linear model to the same perturbation as in Fig. 9: the linear model **A** for a 1-month transition has been applied 16 times to the original perturbation. The excellent correspondence with Fig. 9 indicates that the assumption of linearity for the large scales, and dynamical decoupling between small and large scales, is satisfied in the current model configuration.

$$[\mathbf{x}(\delta t)\ \mathbf{x}(2\delta t)\ \ldots\ ] = \mathbf{A}[\mathbf{x}(0)\ \mathbf{x}(\delta t)\ \ldots\ ] + [\mathbf{q}(0)\ \ldots\ ], \qquad (20)$$

can be solved for the coefficients of **A**. In particular, given the slow propagation speeds of baroclinic Rossby waves in the GCM, it is possible to obtain the reduced-state linear model by computing the response to several density perturbations simultaneously and then solving (20) using a locality constraint. Equation (20) is used to obtain the reduced-order linear model of section 7c.

7. State estimation example

In this final section we present a numerical example of the ocean climate estimation problem making use of the tools and ideas discussed above and providing an opportunity to study the sensitivity of the solution to a priori statistical assumptions. We consider a rectangular piece of ocean in the North Pacific (10°–60°N, 140°–240°E). A 4-yr integration of the Semtner and Chervin (1992) global ocean circulation model with nominal grid spacing of ¼° in the horizontal and 20 levels in the vertical is assumed to represent the real ocean. Pseudo-tomographic and altimetric measurements are then inverted to recover large-scale temperature perturbations about the mean model state. Without loss of generality, a time-invariant system is considered in which **A**, **E**, **Q**, **R**, and **S** are time independent. Vectors $\mathbf{q}(t)$, $\mathbf{n}(t)$, and $\mathbf{x}(t)$ are assumed uncorrelated with each other and with zero mean; $\mathbf{q}(t)$ and $\mathbf{n}(t)$ have zero temporal autocorrelation. The above assumptions are a reasonable starting point, given the coarse spatial and temporal resolution of the reduced state vector. Nevertheless, these assumptions must be checked for statistical consistency with the solution.

The basic model state, $\hat{\boldsymbol{\xi}}(t)$ in (2), is taken to be the 4-yr-mean, depth-integrated temperature of the Semtner and Chervin ocean shown in Fig. 11. The signal, $\mathbf{x}(t)$, consists of 30-day snapshots of temperature perturbations about this 4-yr mean, filtered by operator $\mathbf{B}_h^*\mathbf{B}_v^*$. The model contains several large-scale, westward-propagating Rossby waves, which remain coherent for 2 to 3 years at a time. It is these features that, in combination with the inverse machinery, provide the necessary information for improving estimates of oceanic climate. Figure 12 displays the root-mean-square (rms) variability of $\mathbf{x}(t)$.

a. Ocean acoustic tomography

Ocean acoustic tomography (Munk and Wunsch 1979) provides time series of travel times that are in-

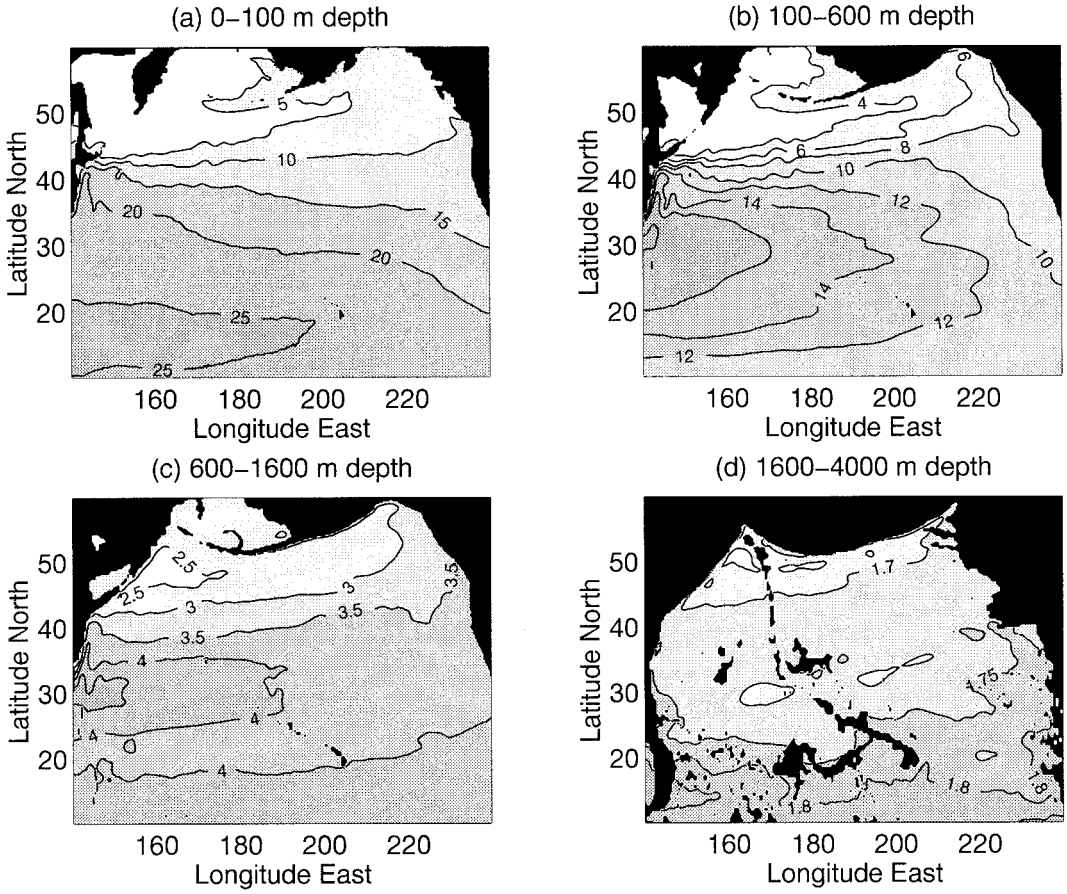

FIG. 11. Four-year depth-integrated temperature mean (°C) of the Semtner and Chervin ocean. In the current numerical example, these fields constitute the basic model state $\hat{\boldsymbol{\xi}}(t)$ in (2).

versely proportional to the integrated along-path sound speed or, equivalently, temperature. Each transmitter–receiver pair can resolve several ray or modal arrivals that have different vertical sampling characteristics. Therefore, the inversion of these arrival times provides some degree of vertical resolution along each path.

In this study the pseudotomographic measurements, $\boldsymbol{\eta}(t)$ in (8), represent the mean temperature perturbation along each of the 13 proposed North Pacific ATOC paths (Fig. 13) at four vertical levels: 0–100, 100–600, 600–1600, and 1600–4000 m. One may think of these as the result of vertical-slice inversions along each path. Figure 14 displays the rms signal $\mathbf{EBx}(t)$ and the noise $\mathbf{n}(t)$ components of the observed difference $\mathbf{y}(t)$ in (10). The simulated measurements have the highest signal-to-noise-ratio in the surface layer, 0–100 m, due to the seasonal heating and cooling of the mixed layer in the model ocean. In practice, we expect poor resolution at the surface (due to the acoustics) and a stronger signal in the lower layers (larger deviation between modeled and true state of the ocean).

Figure 15 shows a contour diagram of a row of matrix $\mathbf{EB}$ corresponding to path 13 in Fig. 13. It represents the measurement model for one of the cross-Pacific ATOC paths. In effect, the measurement model is a weighted average about that path with a decorrelation scale imposed by the coarse representation of $\boldsymbol{\xi}(t)$ by $\mathbf{x}(t)$. The noise term $\mathbf{n}(t)$ is the difference between this weighted average and the mean temperature along the tomographic line, that is, $\mathbf{E}(t)\boldsymbol{\epsilon}(t)$ in (11).

b. Static inversion

A singular value decomposition (e.g., Wunsch 1996) $\mathbf{EB} = \mathbf{U}\boldsymbol{\Lambda}\mathbf{V}^{\mathrm{T}}$ is used to understand the nature of the solution and its relationship to the data. Here, $\mathbf{U}$ is a matrix whose columns span the data space $\mathbf{y}(t)$, $\mathbf{V}$ is a matrix whose columns span the model state space $\mathbf{x}(t)$, and $\boldsymbol{\Lambda}$ is a diagonal matrix of singular values. The current estimation problem is formally underdetermined. There are 52 singular values, and the condition number of $\mathbf{EB}$, the ratio of the largest to the smallest singular value, is 5.9, indicating that all 52 measurements provide independent information about the perturbation field. Consequently, the first 52 columns of $\mathbf{V}$ are said to span the range space of the solution, while the re-

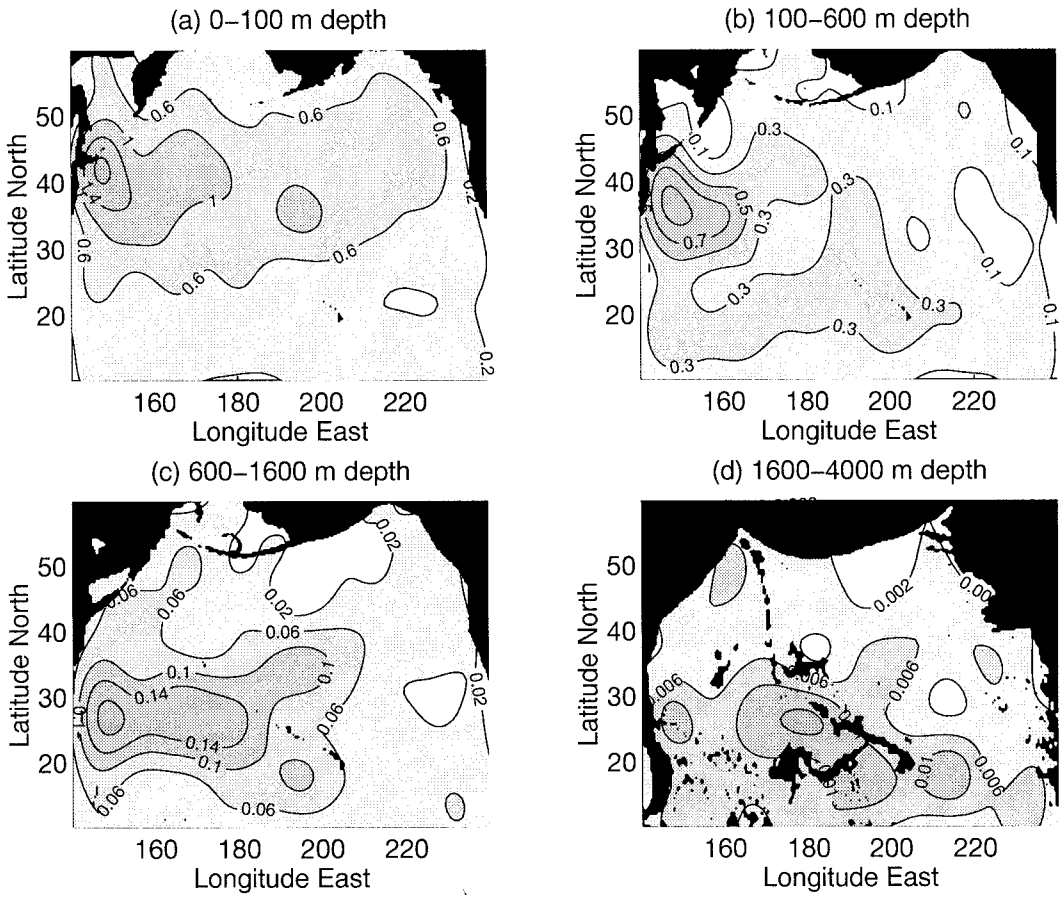

FIG. 12. Standard deviation (°C) of the Semtner and Chervin ocean. Forty-six 30-day snapshots are used, and a 2D FFT filter is applied to eliminate scales smaller than 16° in the horizontal prior to computing the standard deviation. Most of the variability in the top layer is due to the seasonal cycle. As expected, the model variability is maximum near the western boundary.

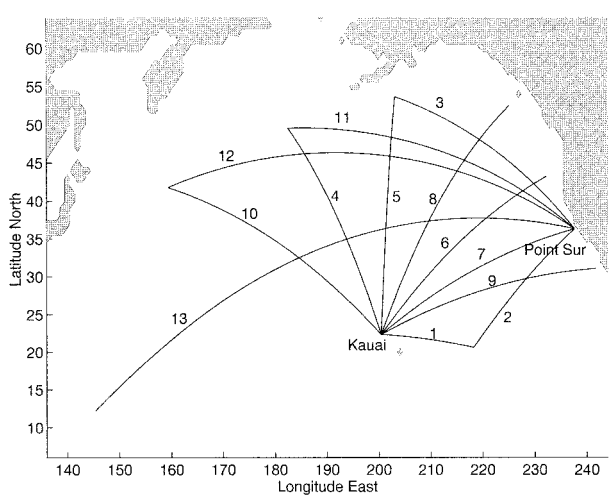

FIG. 13. Proposed ATOC paths in the North Pacific (B. Howe 1994, personal communication). The paths are numbered as a function of increasing range.

maining columns span the null space, about which no information is provided by the measurements.

The singular value decomposition is also a convenient way to obtain the natural solution of the estimation problem, the solution that assumes infinite a priori variance in the range space of the solution and zero variance in the null space. This solution is appropriate when no a priori statistical information is available about the model parameters and the measurements. The corresponding model resolution matrix is $\mathbf{V}_p\mathbf{V}_p^{\mathrm{T}}$, where $\mathbf{V}_p$ is a matrix containing the first 52 columns of $\mathbf{V}$. Diagonal elements of $\mathbf{V}_p\mathbf{V}_p^{\mathrm{T}}$ are plotted in Fig. 16.

Complete lack of a priori knowledge is a very unrealistic scenario—we know, for example, that the Pacific Ocean is not about to evaporate or freeze over. This knowledge can be expressed in the form of a cost function,

$$J = \mathbf{n}^{\mathrm{T}}\mathbf{R}^{-1}\mathbf{n} + \mathbf{x}^{\mathrm{T}}\mathbf{S}^{-1}\mathbf{x}, \tag{21}$$

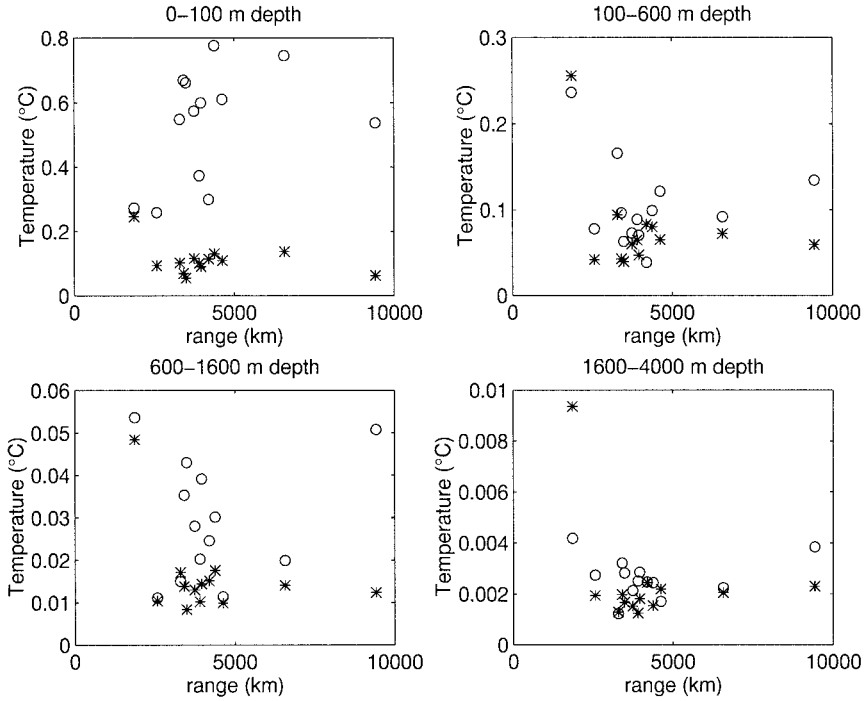

FIG. 14. Standard deviation of signal (circles) and noise (asterisks) for each of the 13 North Pacific ATOC paths as a function of transmission range. The highest signal-to-noise ratio is achieved in the surface layer, because of the strong seasonal signal, and for the longer paths that attenuate mesoscale noise the most.

where a sum squared of measurement residuals and model parameters are weighted by their respective a priori covariance matrices. We inverted the pseudotomographic measurements $\mathbf{y}(t)$ in (10) subject to constraint (21) using the Gauss–Markov estimators for $\mathbf{x}$ and $\mathbf{P}$ (e.g., Wunsch 1996). The inversions were carried out for 46 consecutive snapshots of the Semtner and Chervin ocean at 30-day intervals, and we considered several different a priori $\mathbf{R}$ and $\mathbf{S}$. The figure of merit used to determine the success of the inversion at each point is

$$f_i = \left[1 - \left(\frac{\sum_t [\hat{x}_i(t) - x_i(t)]^2}{\sum_t [x_i(t)]^2}\right)^{1/2}\right] \times 100\%. \quad (22)$$

This represents the explained standard deviation in percent: 100% is perfect resolution, 0% means no improvement, and negative numbers indicate that the solution is worse than the a priori estimate $\langle \mathbf{x} \rangle = 0$.

Figure 17 displays the explained standard deviation at each of the four model levels for a particular inversion where $\mathbf{S}$ and $\mathbf{R}$ are constructed using the actual variance of $\mathbf{x}$ and $\mathbf{n}$ (Figs. 12 and 14, respectively) but with no information about spatial correlations (that is, with zero off-diagonal elements). This result can be compared to the predicted deviation based on solution uncertainty $\mathbf{P}$ and shown in Fig. 18. It is significant that the actual skill of the inversions is somewhat better than that predicted by the uncertainty matrix; that is, the error bars provided by $\mathbf{P}$ are reasonable and somewhat conservative.

The results of Figs. 17 and 18, as well as the results from several other inversions using different a priori statistical assumptions, are summarized in Table 4. A single figure of merit is formed at each level by averaging the explained standard deviation. Table 4 indicates that the skill of the inversions is particularly sensitive to the full and correct specification of the solution covariance matrix $\mathbf{S}$. When $\mathbf{S}$ is fully specified, the inversions can explain up to 60% of the rms signal as opposed to 8% with a diagonal $\mathbf{S}$. The importance of the off-diagonal elements of $\mathbf{S}$ relative to the off-diagonal elements of $\mathbf{R}$ is not surprising given that the dimension of $\mathbf{S}$ is 512 as compared to the dimension of $\mathbf{R}$, which is 52; Therefore, $\mathbf{S}$ imposes 100 times more constraints than $\mathbf{R}$ in (21). The importance of the off-diagonal elements of $\mathbf{S}$ also indicates that there is considerable spatial correlation between the elements of the state vector, that is, the spatial spectrum of $\mathbf{x}(t)$ is red. In practice, the a priori statistics can be provided by a recent climatology of the region under study or by a realistic GCM, but we do not expect the skill of the inversions to ever approach that indicated by the bottom two rows of Table 4. However, with enough data, adap-

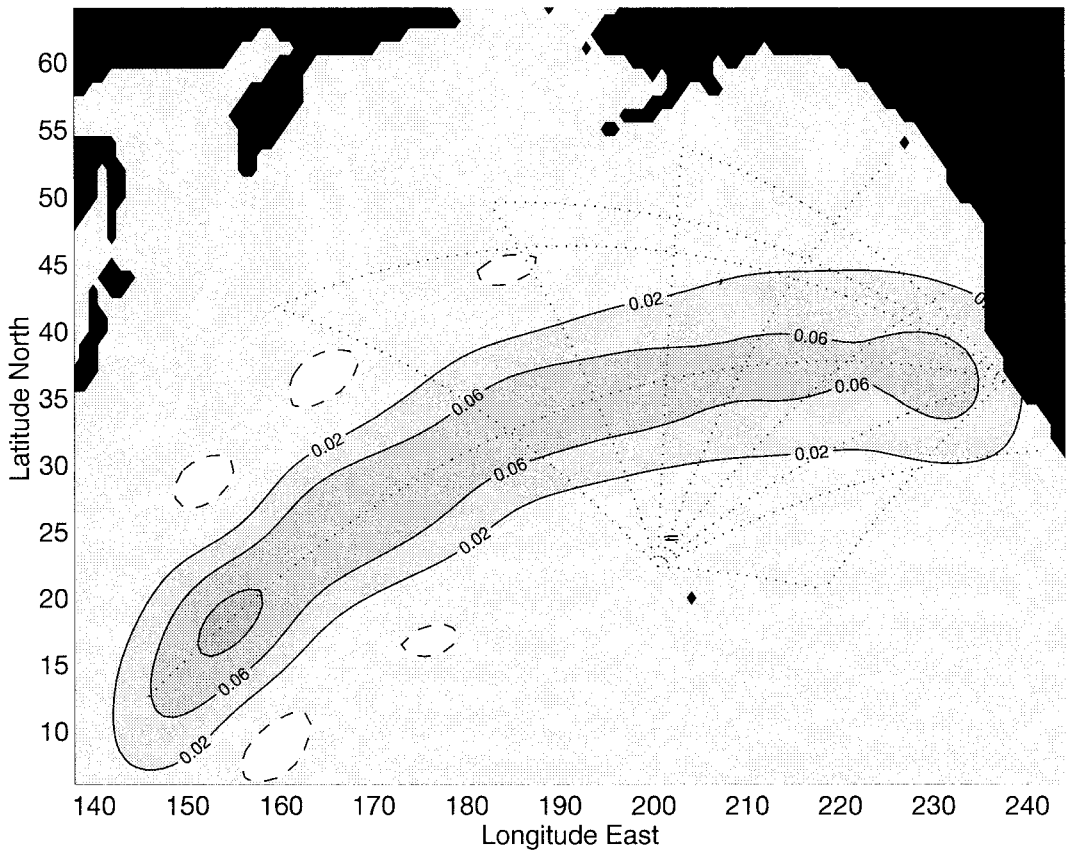

FIG. 15. Contour plot of measurement model for the cross-Pacific path 13 in Fig. 13. The measurement model is an areal average of temperature with a cross-path width imposed by the coarse representation of the perturbation field. As discussed in the text, the measurement error is taken to be the difference between this areal average and the line-averaged temperature along the path. The contours are dimensionless and are scaled so that they represent a unit perturbation of the corresponding measurement.

tive filter/smoother methods could be used to determine the model and data covariances.

c. Time-dependent inversion

We use (20) and a singular value decomposition keeping 25 singular values to derive the state-transition matrix that is used in the numerical example below. The time-dependent inverse solution here seeks to minimize a weighted sum of initial conditions, measurement residual, and process noise:

$$J = \mathbf{x}^{\mathrm{T}}(0)\mathbf{S}^{-1}\mathbf{x}(0) + \sum_{t} [\mathbf{n}^{\mathrm{T}}(t)\mathbf{R}^{-1}\mathbf{n}(t) + \mathbf{q}^{\mathrm{T}}(t)\mathbf{Q}^{-1}\mathbf{q}(t)], \tag{23}$$

which is equivalent to solving the complete set of equations,

$$\begin{bmatrix} \mathbf{y}(0) \\ \mathbf{y}(1) \\ \vdots \\ \mathbf{y}(k) \end{bmatrix} = \begin{bmatrix} \mathbf{EB} & \cdots & \mathbf{O} \\ \mathbf{O} & \mathbf{EB} \cdots & \mathbf{O} \\ & \ddots & \\ \mathbf{O} & \cdots & \mathbf{EB} \end{bmatrix} \begin{bmatrix} \mathbf{A}^0 & \cdots & \mathbf{O} \\ \mathbf{A}^1 & \mathbf{A}^0 \cdots & \mathbf{O} \\ & \ddots & \\ \mathbf{A}^k & \cdots & \mathbf{A}^0 \end{bmatrix} \begin{bmatrix} \mathbf{x}(0) \\ \mathbf{q}(1) \\ \vdots \\ \mathbf{q}(k) \end{bmatrix} + \begin{bmatrix} \mathbf{n}(0) \\ \mathbf{n}(1) \\ \vdots \\ \mathbf{n}(k) \end{bmatrix}. \tag{24}$$

As discussed in the appendix, this equation is equivalent to Eq. (14) in Stammer and Wunsch (1996). The filter/smoother formalism provides an efficient sequential algorithm for minimizing (23). We use the Kalman filter

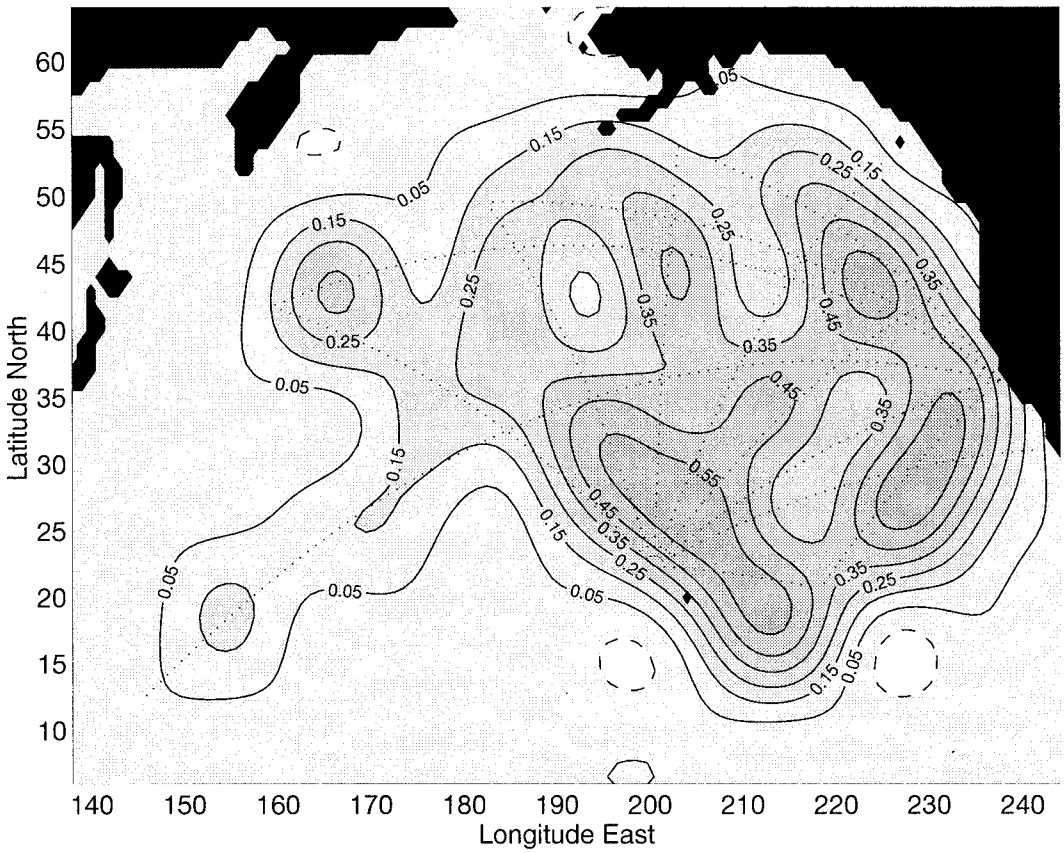

FIG. 16. Diagonal elements of the model resolution matrix for the natural solution that assumes infinite variance in the range space of the measurements and zero variance in the null space. The amount by which the resolution differs from 1 indicates the spread of the solution into adjacent areas.

in combination with the fixed-interval Rauch–Tung–Striebel smoother (e.g., Gaspar and Wunsch 1989).

The sensitivity of the filter/smoother to a priori statistical assumptions was tested for several combinations of **R**, **Q**, and **S**. Some results are summarized in Table 5. We find that diagonal covariance matrices are very poor assumptions and that they degrade the estimates compared to the static inversion. We also find that the inversion is somewhat more sensitive to the correct a priori specification of measurement residual **R** than it is to that of process noise **Q**. This result is encouraging because the correct characterization of process noise is the most challenging task in practice.

To avoid divergence of the smoothed estimates from the true solution for poor a priori **R**, **S**, and **Q**, additional data constraints are required. In the absence of sufficient data, an alternative approach is to require the solution to remain within some reasonable bounds, which could be provided by a recent climatology or otherwise. This can be achieved by minimizing the cost function,

$$J = \sum_t [\mathbf{x}^{\mathrm{T}}(t)\mathbf{S}^{-1}\mathbf{x}(t) + \mathbf{n}^{\mathrm{T}}(t)\mathbf{R}^{-1}\mathbf{n}^{\mathrm{T}}(t) + \mathbf{q}^{\mathrm{T}}(t)\mathbf{Q}^{-1}\mathbf{q}(t)], \tag{25}$$

instead of (23). This cost function requires the solution to remain consistent with the a priori covariance matrix **S** at every time step. In the filter/smoother formalism, it is possible to minimize (25) by adding ''synthetic'' measurements to Eq. (10),

$$\begin{bmatrix} \mathbf{y}(t) \\ \mathbf{O} \end{bmatrix} = \begin{bmatrix} \mathbf{EB} \\ \mathbf{I} \end{bmatrix} \mathbf{x}(t) + \begin{bmatrix} \mathbf{n}(t) \\ -\mathbf{x}(t) \end{bmatrix}, \tag{26}$$

with error covariance matrix,

$$\mathbf{R}_s = \begin{bmatrix} \mathbf{R} & \mathbf{O} \\ \mathbf{O} & \mathbf{S} \end{bmatrix}. \tag{27}$$

Figures 19 and 20 display results of a time-dependent inversion using synthetic measurements for diagonal a priori **Q**, **R**, and **S**. Further results are summarized in Table 6. Clearly, the synthetic measurements vastly improve estimates of the solution $\mathbf{x}(t)$, as compared to the results reported on Tables 4 and 5. Unfortunately, for wrong a priori **S**, this formulation tends to underestimate the magnitude of the error covariance matrix **P**.

d. Satellite altimetry

The inversion methods discussed in the previous section can accommodate most other types of measure-

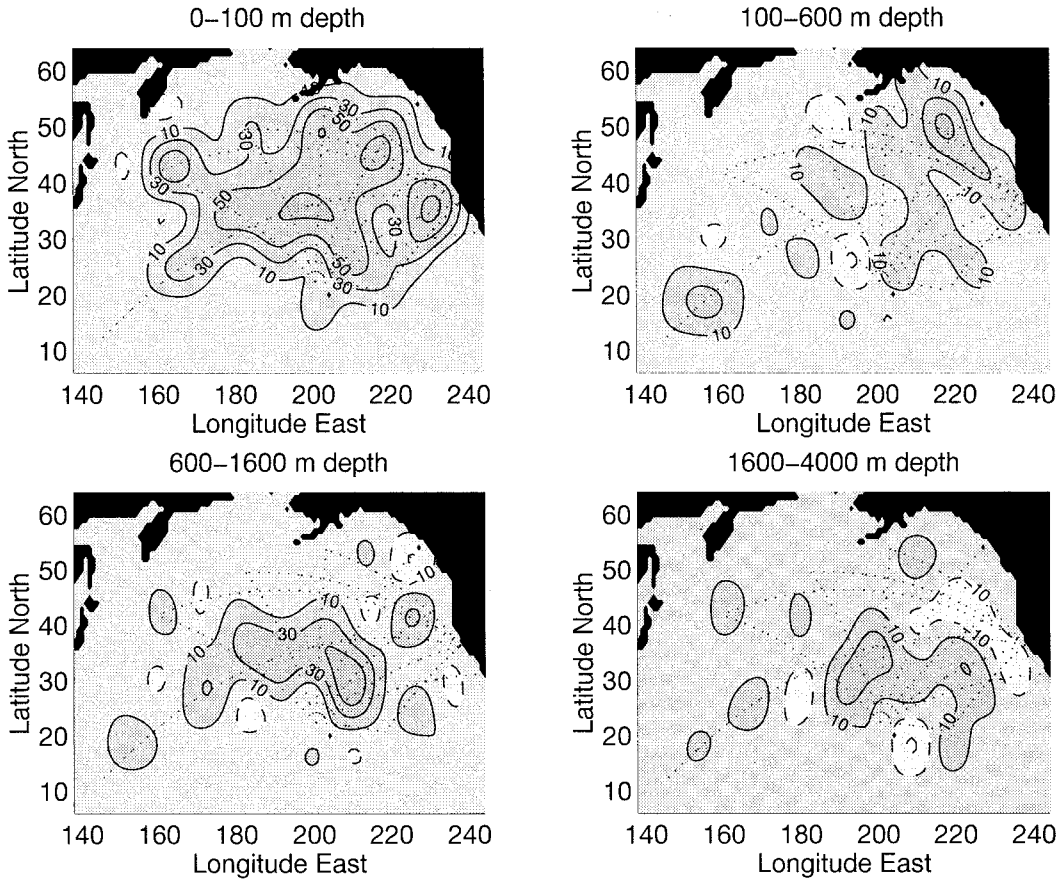

FIG. 17. Explained standard deviation in percent for a static inversion using pseudotomographic measurements: 100% is perfect resolution, 0% means no improvement, and negative numbers indicate the solution is worse than the a priori estimate. Diagonal a priori measurement residual, and solution covariance matrices were used. These impose the correct variance but wrongly assume zero spatial correlation. The estimates are best in the surface layer where the measurements have the highest signal-to-noise ratio.

ments, so long as a linear model relating the measurements to the state vector $\mathbf{x}(t)$ can be established. The particular case of satellite altimetry is discussed in this section. Assuming that the large-scale perturbations of the ocean relative to model predictions are in geostrophic and hydrostatic balance, then the sea surface elevation can be decomposed into a steric component plus an integration constant. The integration constant is proportional to the horizontal gradient of the depth-averaged velocity, and to first order it is not seen by one-way tomography. The steric component is the full-water column integral of density perturbations, $\rho(x, y, z, t)$, producing a sea surface elevation

$$h(x, y, t) = \frac{-1}{\rho_0(x, y, t)} \int_{-H(x,y)}^{0} \rho(x, y, z, t)\, dz, \quad (28)$$

where $H(x, y)$ is the depth of the water column and $\rho_0(x, y, t)$ is the seawater density at the surface. For example, a 0.5°C warming of a layer between 100- and 600-m depth with mean salinity 34.7 psu and temperature 9.6°C results in a 4.3-cm sea surface elevation (see Table 7). The current definition of the state reduction operator $\mathbf{B}^*$ filters out variability due to barotropic Rossby waves (see section 5). There remain barotropic perturbations caused by readjustments to changing surface boundary conditions that have not been adequately predicted by the GCM. These become part of the measurement error, $\mathbf{E}(t)\boldsymbol{\epsilon}(t)$ in (11), because they cannot be resolved by the reduced state vector.

Pseudoaltimetric measurements were constructed in the Semtner and Chervin ocean using the values of dh/dT from Table 7 and 1-cm rms Gaussian residuals, typical of TOPEX/Poseidon sea level anomaly error for the large spatial and temporal scales considered here. The results of some static and time-dependent inversion experiments making use of these pseudoaltimetric measurements are summarized in Table 8. The results of these idealized experiments indicate that overall altimetry is the richest and most useful signal, even for the deep levels. This is not surprising given the limited number of tomographic integrals as compared to the complete spatial coverage of the altimeter. Nevertheless,

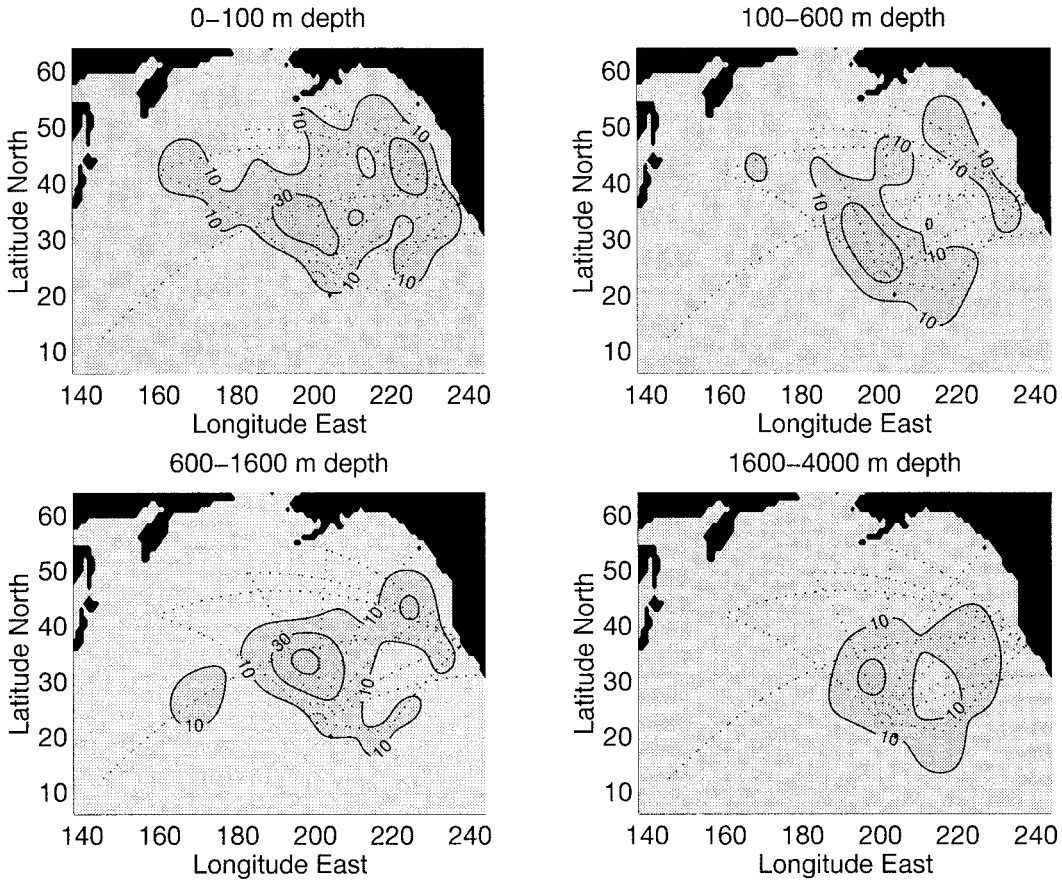

FIG. 18. Explained standard deviation predicted using the error covariance matrix **P** for the same experiment as that of Fig. 17. A comparison of Figs. 17 and 18 shows that the actual skill of the inversions is, in general, better than or similar to the predicted skill.

the combination of altimetric and tomographic measurements improves the overall skill of the inversions relative to that of either measurement on its own. It should also be pointed out that the assumption of white noise for the altimeter measurements may be unrealistic and that long-term climate-scale changes are unlikely to have the linear physics assumed here. Tomographic integrals measure temperature directly and can therefore help to ground-truth altimetry, to diagnose ageostrophic adjustments, and to separate the measured sea surface elevation into barotropic and steric components. For the reasons discussed earlier, the filter/smoother with synthetic measurements outperforms the other two types of inversions but underestimates the uncertainty of the es-

TABLE 4. Actual and predicted explained standard deviation for static inversions using pseudotomographic measurements. Each number represents the mean explained deviation in percent at a particular level. A priori statistics are obtained here from the known **x** and **n**, but off-diagonal information is withheld in some of the examples as indicated. The second row of the table (diagonal **R**, **S**) summarizes the results of Figs. 17 and 18. Various other combinations of **R** and **S** are considered. The results improve as the a priori statistics supplied to the inversion become more realistic. Except for the natural solution, which assumes infinite variance in the range space of the measurements, and zero in the null space, the error covariance matrices are generally consistent with the observed error.

	Explained standard deviation (%)							
	Actual				Predicted using **P**			
Level (m)	100	600	1600	4000	100	600	1600	4000
Natural solution	5	−12	−11	−12	37	36	39	39
Diagonal **R**, **S**	18	5	5	3	6	5	5	4
Full **R**, diagonal **S**	19	8	7	5	8	7	7	7
Diagnoal **R**, full **S**	67	61	57	58	70	64	61	62
Full **R**, **S**	88	87	86	86	88	87	86	85

TABLE 5. Actual and predicted explained standard deviation for filter/smoother inversions using pseudotomographic measurements. These results can be compared with those for the static inversions reported in Table 4. The skill of the time-dependent estimates is worse than that of the static inversions when incomplete a priori **Q** and **R** are supplied. As discussed in the text, the divergence of the estimates from the actual solution results from insufficient data constraints.

	Explained standard deviation (%)							
	Actual				Predicted using **P**			
Level (m)	100	600	1600	4000	100	600	1600	4000
Diagonal **R**, **Q**, **S**	13	7	−9	−9	−24	0	−19	−27
Diagonal **R, S,** full **Q**	24	20	5	11	0	15	1	−5
Full **R**, **S**, diagonal **Q**	20	29	8	5	20	41	28	20
Full **R**, **S**, **Q**	96	97	96	96	90	92	90	86

timates. More realistic a priori covariance matrices, instead of the diagonal matrices used for constructing Table 8, improve the results substantially.

8. Concluding remarks

The principal contributions of this study are the evaluation of the MIT GCM response to large-scale internal density perturbations in a North Pacific test basin, and the recipe for obtaining and using a reduced-order linearized model to estimate ocean climate. At midlatitudes, the model response is that of linear baroclinic Rossby waves, modified by complex interactions with horizontal density gradients, mean advection velocity, and, to a lesser extent, topography (see Figs. 7 and 8). Except near the western boundary, the model response to a localized perturbation is essentially similar on the large scales to that resulting from a large-scale initial pertur-

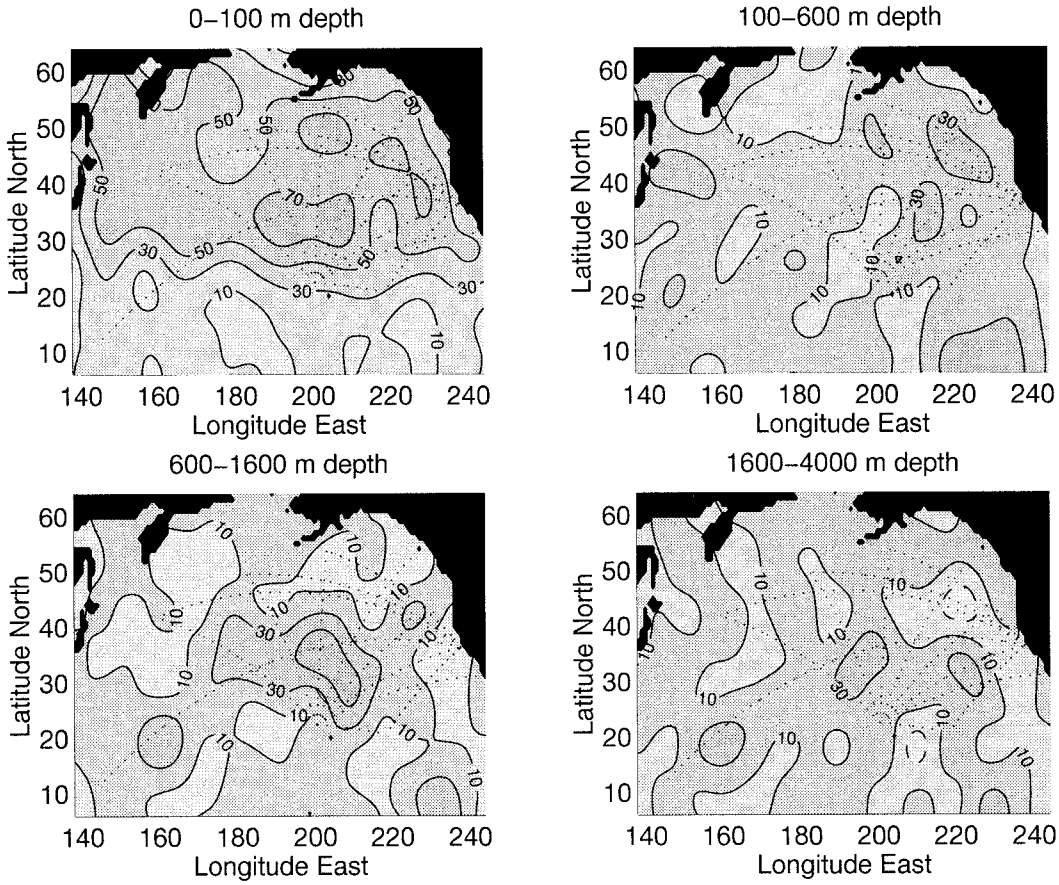

FIG. 19. Explained standard deviation in percent for a time-dependent inversion using pseudotomographic measurements. Diagonal a priori system error, measurement residual, and solution covariance matrices were used. Notice the overall improvement as compared to the results of the static inversion of Fig. 17. As discussed in the text, the solution is constrained to consistency with **S** at every time step. This overcomes the divergence problems reported in Table 5.

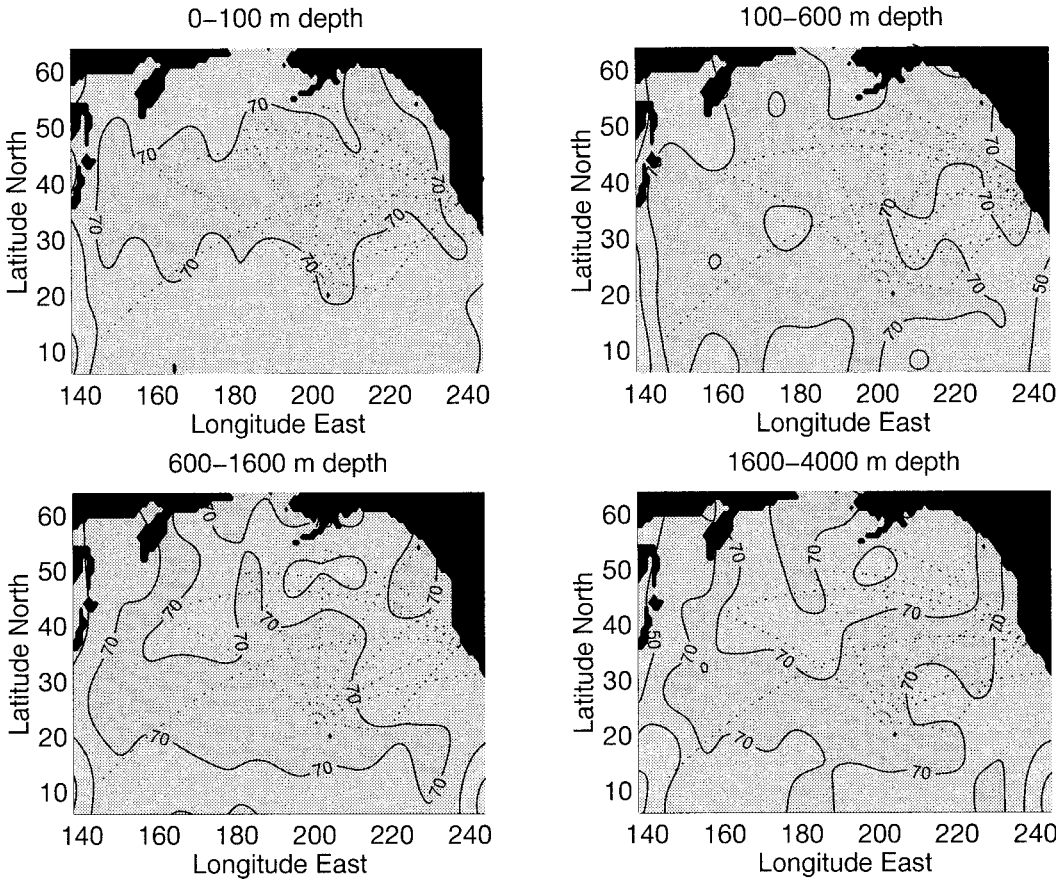

FIG. 20. Explained standard deviation predicted using the error covariance matrix **P** for the same experiment as that of Fig. 19. The predicted errors are everywhere smaller than the actual errors (the predicted skill is higher than the actual skill of Fig. 19). This problem results from insufficient data constraints and wrong a priori statistical assumptions in the current experiment.

bation. This result indicates that the large-scale model response is largely decoupled from the smaller and faster model physics.

Two methods for obtaining a reduced-order linear model that describe the evolution of the large-scale internal density perturbations have been described. The first method is based on the computation of model Green's functions and their representation in state-transition matrix form. The second is a form of principal oscillation pattern analysis. The reduced-order linear model compares favorably with the large-scale response of the fully nonlinear GCM for a period of up to 2 years (see Figs. 9 and 10). The linear model is suitable for climate estimation studies. Numerical examples of both static and time-dependent inversions have been presented using simulated tomographic and altimetric measurements. As a result of insufficient data constraints, the inversions are extremely sensitive to the quality of the a priori statistical assumptions.

The following algorithmic improvements are sug-

TABLE 6. Actual and predicted explained standard deviation for filter/smoother inversions using pseudotomographic measurements and constrained to consistency with **S** at every time step. The current estimates are considerably better than those reported in Tables 4 and 5. However, the error covariance matrix underestimates the errors when incomplete a priori **S** is supplied.

	Explained standard deviation (%)							
	Actual				Predicted using **P**			
Level (m)	100	600	1600	4000	100	600	1600	4000
Diagonal **R**, **Q**, **S**	41	17	17	14	67	72	69	67
Diagonal **R**, **S**, full **Q**	48	29	26	27	82	84	82	81
Full **R**, **S**, diagonal **Q**	93	94	93	93	96	96	96	96
Full **R**, **S**, **Q**	96	96	96	96	96	96	96	96

TABLE 7. Typical values for sea surface elevation due to large-scale temperature perturbations in hydrostatic and geostrophic balance.

Layer depths (m)	0–100	100–600	600–1600	1600–4000
Mean S (psu)	34.7	34.7	34.7	34.7
Mean T (°C)	14.2	9.6	3.6	1.7
Mean ρ (kg m^{-3})	1026	1028	1033	1041
ΔT (°C)	1.0	0.5	0.1	0.01
$\Delta\rho$ (kg m^{-3})	−0.2172	−0.0878	−0.0127	−0.0015
Δh (cm)	2.1	4.3	1.2	0.34
$d\rho/dT$ (kg m^{-3} °C^{-1})	−0.2125	−0.1730	−0.1261	−0.1477
dh/dT (m °C^{-1})	0.0207	0.0841	0.1221	0.3406

gested. For large-scale, low-frequency estimates of oceanic circulation, model Green's functions can be initialized using internal density perturbations, instead of vortices as in Stammer and Wunsch (1996). The former excite a predominantly baroclinic response, have much longer persistence, and are easier to implement numerically. Because most of the energy of long planetary waves is in potential form, the initial geostrophic adjustment transients can be neglected. By contrast, the adjustment process cannot be neglected when the perturbations are initialized from vortices. This adjustment adds to the computational burden of the model Green's functions as it may take up to a full month for the geostrophic adjustment transients to die down. Most of the useful information about the interior of the ocean is contained in the baroclinic response (see Fig. 8). The depth-integrated response, which is not excited by the method proposed here, is predominantly a function of bottom topography and surface wind forcing.

The state-transition matrix provides an efficient representation of model Green's functions. This representation substantially reduces processing and storage costs (see the appendix). It naturally lends itself to the use of sequential estimation algorithms. Therefore, much larger inverse problems can be tackled with the same computational resources. Given the slow propagation of baroclinic information in the ocean, it is suggested that the response to several perturbations can be computed simultaneously, thus further reducing processing requirements. Equation (19) or (20) is then used to obtain the state-transition matrix.

Due to insufficient data constraints and imperfect knowledge of a priori statistics, the estimates provided by the time-dependent inversion can diverge from the desired solution. A simple modification of the problem formulation, Eqs. (25)–(27), can be used to require the solution to remain within bounds provided by a recent climatology or otherwise.

Important issues that have not been addressed in this study include the optimal choice of a priori covariance matrices for the oceanic state vector, measurement residuals, and system errors. Our priorities for future work are the application of the above ideas to real data, and the testing of reduced-order linear models in other basins and at higher GCM resolutions.

Acknowledgments. We gratefully acknowledge the help of the MIT GCM team: Alistair Adcroft, Curtis Heisey, Chris Hill, John Marshall, and Lev Perelman. This study benefited from discussions with our col-

TABLE 8. Actual and predicted explained standard deviation for static and time-dependent inversions using pseudoaltimetric and pseudotomographic measurements. Diagonal a priori **Q**, **R**, and **S** are assumed throughout.

	Explained standard deviation (%)							
	Actual				Predicted using **P**			
Level (m)	100	600	1600	4000	100	600	1600	4000
Static inversions								
Tomography	18	5	5	3	6	5	5	4
Altimetry	20	39	14	3	12	28	4	0
Altimetry and tomography	31	43	18	5	17	32	8	4
Filter/smoother								
Tomography	13	7	−9	−9	−24	0	−19	−27
Altimetry	29	53	22	10	0	29	−17	−32
Altimetry and tomography	37	55	25	11	9	35	−6	−22
Filter/smoother with synthetic measurements								
Tomography	41	17	17	14	67	72	69	67
Altimetry	52	57	40	34	69	76	69	67
Altimetry and tomography	63	61	45	37	71	77	70	68

leagues Ichiro Fukumori, Jochem Marotzke, and Detlef Stammer. We thank Bert Semtner and Bob Chervin for making their model output available. Financial support was provided by SERDP/DARPA as part of the ATOC project (University of California SIO Contract PO#10037358) and by NASA Grant NAGW 1048. This work was also supported by grants of HPC time from Project SCOUT at MIT-LCS (DARPA Contract MDA972-92-J-1032), from the Arctic Region Supercomputing Center, and from the Scientific Computing Division of the National Center for Atmospheric Research.

APPENDIX

Efficient Representation of Green's Functions

Because of the linearity assumption, the Green's functions computed in section 4 or in Wunsch (1985) and Stammer and Wunsch (1996) can be efficiently represented by a state-transition matrix. The model Green's function $G_{ij}(t)$ is defined as the time-evolving model response at location i and time t caused by a unit perturbation at location j and time 0. Subscripts i and j can also refer to some truncated basis set, as discussed in section 5, and t is the corresponding time index. If the perturbation physics of the model are approximately linear for the resolved scales, then by definition

$$G_{ij}(t) = \sum_{k=1}^{N} G_{ik}(1)G_{kj}(t-1), \tag{A1}$$

where N is the state dimension. The state transition matrix is defined as

$$\mathbf{A} = \begin{bmatrix} G_{11}(1) & \cdots & G_{1N}(1) \\ \vdots & & \\ G_{N1}(1) & \cdots & G_{NN}(1) \end{bmatrix}. \tag{A2}$$

Equations (A1) and (A2) yield

$$\begin{bmatrix} G_{1j}(t) \\ \vdots \\ G_{Nj}(t) \end{bmatrix} = \mathbf{A}^t \begin{bmatrix} G_{1j}(0) \\ \vdots \\ G_{Nj}(0) \end{bmatrix}, \tag{A3}$$

where $G_{ij}(0) = 1$ for $i = j$, and 0 otherwise. Therefore Eq. (14) in Stammer and Wunsch (1996) is seen to be equivalent to (24) in this paper. This representation of the Green's functions affords more than an order of magnitude decrease in the computational cost and storage requirements. The model response to each perturbation needs be computed for a single time step, rather than for the complete duration of the experiment. The response at future time steps can then be constructed using (A3) as shown on Figs. 9 and 10. Furthermore, the inverse problem can now be solved sequentially using filter/smoother algorithms as was done in section 7.

Specifically, the computation of the state-transition matrix requires integrating the GCM for a total of N linear model time steps and the storage requirement for $\mathbf{A}$ is N^2. The computation of the complete set of model Green's functions requires integrating the GCM for a period of $\Sigma_i^M K_i t_f$ and the storage requirement is $\Sigma_i^M K_i N t_f/\delta t$, where M is the total number of measurements, t_f is the duration of the experiment, and δt is the linear model time step. Here, K_i represents the number of degrees of freedom assigned to measurement i, that is, the number of nonzero elements for the particular row of $\mathbf{EB}$ in (10) corresponding to the given measurement. A separate Green's function must be computed for each degree of freedom. In general, point measurements have a single degree of freedom, while integrating measurements such as altimetry or tomography have several.

For the example of section 7d, $N = 336$, $\Sigma_i^M K_i \sim 800$, $t_f = 46$ months, and $\delta t = 1$ month. Therefore the storage requirement for the state transition matrix is $N^2 \sim 10^5$ as opposed to $\Sigma_i^M K_i N t_f/\delta t \sim 10^7$ for the complete set of Green's functions. The computation of the state transition matrix requires $N\delta t = 28$ GCM years as opposed to $\Sigma_i^M K_i t_f = 3066$ GCM years for the complete set of Green's functions.

REFERENCES

Bennett, A. F., 1992: *Inverse Methods in Physical Oceanography. Cambridge Monographs on Mechanics and Applied Mathematics.* Cambridge University Press, 346 pp.

Bindoff, N. L., and C. Wunsch, 1992: Comparison of synoptic and climatologically mapped sections in the South Pacific Ocean. *J. Climate,* **5,** 631–645.

Blumen, W., 1972: Geostrophic adjustment. *Rev. Geophys. Space Phys.,* **10** (2), 485–528.

Bryan, K., 1969: A numerical method for the study of the circulation of the world ocean. *J. Comput. Phys.,* **4,** 347–376.

Cox, M. D., 1984: A primitive equation, three-dimensional model of the ocean. GFDL Ocean Group Tech. Rep. 1, Geophysical Fluid Dynamics Lab, Princeton, NJ, 143 pp. [Available from Geophysical Fluid Dynamics Laboratory/NOAA, Princeton University, Princeton, NJ 08542.]

Fukumori, I., and C. Wunsch, 1991: Efficient representation of the North Atlantic hydrographic and chemical distributions. *Progress in Oceanography,* Vol. 27, Pergamon Press, 111–195.

——, and P. Malanotte-Rizzoli, 1995: An approximate Kalman filter for ocean data assimilation: An example with an idealized Gulf Stream model. *J. Geophys. Res.,* **100,** 6777–6793.

Gaspar, P., and C. Wunsch, 1989: Estimates from altimeter data of barotropic rossby waves in the northwestern Atlantic Ocean. *J. Phys. Oceanogr.,* **19,** 1821–1844.

Ghil, M., and P. Malanotte-Rizzoli, 1991: Data assimilation in meteorology and oceanography. *Advances in Geophysics,* Vol. 33, Academic Press, 141–266.

Gill, A. E., 1982: *Atmosphere-Ocean Dynamics.* International Geophysics Series, Vol. 30, Academic, 662 pp.

Levitus, S., 1982: *Climatological Atlas of the World Ocean.* National Oceanic and Atmospheric Administration, 173 pp. and 17 microfiche.

——, 1990: Interpentadal variability of steric sea level and geopotential thickness of the North Atlantic Ocean, 1970–1974 versus 1955–1959. *J. Geophys. Res.,* **95** (C4), 5233–5238.

——, J. I. Antonov, and T. P. Boyer, 1994: Interannual variability of

temperature at a depth of 125 meters in the North Atlantic Ocean. *Science,* **266,** 96–99.

Malanotte-Rizzoli, P., and R. E. Young, 1992: How useful are localized clusters of traditional oceanographic measurements for data assimilation? *Dyn. Atmos. Oceans,* **17,** 23–61.

Marotzke, J., and C. Wunsch, 1993: Finding the steady state of a general circulation model through data assimilation: Application to the North Atlantic Ocean. *J. Geophys. Res.,* **98** (C11), 20 149–20 167.

Marshall, J., A. Adcroft, C. Hill, L. Perelman, and C. Heisey, 1997a: A finite-volume, incompressible Navier–Stokes model for studies of the ocean on parallel computers. *J. Geophys. Res.,* **102**(C3), 5753–5766.

——, C. Hill, L. Perelman, and A. Adcroft, 1997b: Hydrostatic, quasi-hydrostatic and non-hydrostatic ocean modeling. *J. Geophys. Res.,* **102**(C3), 5733–5752.

Munk, W., and C. Wunsch, 1979: Ocean acoustic tomography: A scheme for large scale monitoring. *Deep-Sea Res.,* **26A,** 123–161.

Oberhuber, J. M., 1988: An atlas based on the 'COADS' data set: The budgets of heat, buoyancy and turbulent kinetic energy at the surface of the global ocean. Max-Plank Institute for Meteorology Rep. 15, 20 pp. [Available from Max-Plank Institute for Meteorology, Bundesstrasse 55, 2000 Hamburg 13, Germany.]

Parrilla, G., A. Lavín, H. Bryden, M. García, and R. Millard, 1994: Rising temperatures in the subtropical North Atlantic Ocean over the past 35 years. *Nature,* **369,** 48–51.

Philander, S. G. H., 1978: Forced oceanic waves. *Rev. Geophys. Space Phys.,* **16** (1), 15–46.

Pickard, G. L., and W. J. Emery, 1990: *Descriptive Physical Oceanography.* 5th ed. Pergamon, 320 pp.

Pond, S., and G. L. Pickard, 1983: *Introductory Dynamical Oceanography.* 2d ed. Pergamon, 329 pp.

Roemmich, D., 1992: Ocean warming and sea level rise along the southwest U.S. coast. *Science,* **257,** 373–375.

Semtner, A. J., Jr., and R. M. Chervin, 1992: Ocean general circulation from a global eddy-resolving model. *J. Geophys. Res.,* **97** (C4), 5493–5550.

Stammer, D., and C. Wunsch, 1996: The determination of the the large-scale circulation of the Pacific Ocean from satellite altimetry using model Green's functions. *J. Geophys. Res.,* **101**(C8), 18 409–18 432.

Trenberth, K. E., J. G. Olson, and W. G. Large, 1989: A global ocean wind stress climatology based on ECMWF analyses. NCAR Tech. Note NCAR/TN-338+STR, 93 pp. [Available from National Center for Atmospheric Research, Boulder, CO 80307.]

von Storch, H., 1993: Principal oscillation pattern analysis of the intraseasonal variability in the equatorial Pacific Ocean. *'Aha Huliko'a Proceedings,* P. Müller and D. Henderson, Eds., School of Ocean and Earth Sciences and Technology, University of Hawaii, 201–227.

Wunsch, C., 1985: Eclectic modelling of the North Atlantic. II. Transient tracers and the ventilation of the eastern basin thermocline. *IEEE J. Oceanic Eng.,* **OE-10** (2), 123–136.

——, 1996: *The Ocean Circulation Inverse Problem.* Cambridge University Press, 442 pp.